https://ntrs.nasa.gov/search.jsp?R=19960011794 2019-04-30T06:49:53+00:00Z

N96- 70679

The Effect of Laser Pulse Tailored Welding of Inconel 718†

T. Dwayne McCay,‡ Mary Helen McCay,* C. Michael Sharp,** and Michael G. Womack***

Center for Advanced Space Propulsion
University of Tennessee Space Institute
Tullahoma, Tennessee 37388
USA

Abstract

Pulse tailored laser welding has been applied to wrought, wrought grain grown and cast Inconel 718 using a CO_2 laser. Prior to welding, the material was characterized metallographically and the solid state transformation regions were identified using Differential Scanning Calorimetry and high temperature x-ray diffraction. Bead on plate welds (restrained and unrestrained) were then produced using a matrix of pulse duty cycles and pulsed average power. Subsequent characterization included heat affected zone width, penetration and underbead width, the presence of cracks, microfissures and porosity, fusion zone curvature, and precipitation and liquated region width. Pedigree welding on three selected processing conditions was shown by microstructural and dye penetrant analysis to produce no microfissures, a result which strongly indicates the viability of pulse tailored welding for microfissure free IN 718.

I. Introduction

Inconel 718 was developed over thirty years ago by the International Nickel Company. Since that time its use has grown until it accounts for thirty-five percent of superalloy production.[1] Due to its exceptional properties from cryogenic temperatures up to 650° C, the material is routinely employed in gas turbine disks for resistance to creep and stress rupture at elevated temperature and in cryogenic piping for environmental cracking resistance. Additional uses are continually being developed as techniques for processing and fabricating the alloy advance.

Welding is one of the more desirable fabrication techniques for turbine and aircraft engine components and hence has been seriously investigated for IN 718. The main problem is microfissuring and cracking although the reduction of properties in the heat affected zone (HAZ) is also a concern. Common welding techniques are[2] shielded-metal arc, gas-tungsten arc, gas-metal arc, resistance, and electron beam. The common requirement for these processes is that they use minimal heat input in order to prevent cracking. Since laser welding uses a very localized heat source and produces a narrow heat affect zone (similar to electron beam welding), it has recently begun to be investigated as a technique for joining IN 718.

The purpose of this report is to present the results of recent studies and analyses of laser pulse tailored welding on three microstructures of Inconel; wrought, wrought-grain grown, and cast.

II. Background

Alloy 718 is known as a nickel-iron base alloy. Its nominal composition is 53% Ni, 18.6% Cr, 18.5% Fe, 3.1% Mo, 5% Nb, 0.4% Al, 0.9% Ti, 0.2% Mn, 0.3% Si and 0.04% C. The matrix is austenitic and the major strengthening components are gamma double prime (Ni_3Nb,Al), an ordered body centered tetragonal phase, and gamma prime (Ni_3Al,Nb) which is a face centered cubic phase. Although they are both primarily nickel, the gamma double prime is richer in niobium while the gamma prime is richer in aluminum. Other phases of significance which occur in present day alloys are delta (Ni_3Nb), Laves (A_2B) and MC.[1] Time-temperature-precipitation (TTP) diagrams have been developed by a number of investigators[3,4,5] to describe the formation of these phases in IN 718. A composite of those results is shown in Figure 1.[2] The state of the alloy can shift the curves to the right or the left, hence differences in grain size or thermal history can produce differences in phase formation.

Although Alloy 718 was originally developed as a wrought alloy, increasing need for its properties has resulted in its recent use as an investment casting alloy. In this form, the microstructure is significantly different from the wrought as can be seen from the

† This work was supported in part by the UT-Calspan Center for Advanced Space Propulsion under NASA Grant No. NAGW-1195.

‡ Professor, Engineering Science & Mechanics, Principal Investigator, UTSI

* Associate Professor, Engineering Science & Mechanics, UTSI

** Processing Engineer, UTSI

*** Graduate Research Assistant, UTSI

comparisons in Figure 2. There is significant concentration of niobium in the Laves phase (Ni_3Nb) eutectic which forms interdendritically and in the grain boundaries. The extensive niobium segregation is extremely difficult to eliminate by thermal treatment[6]. As would be expected, this creates difficulties in processes such as welding when going from wrought to cast material.

During the welding of Alloy 718, microfissures often occur in the heat affected zone creating problems in fabrication and repair. The microfissures are generally thought to be due to the combination of welding stresses and liquation, a phenomena that is influenced by microstructure and constituent inhomogeneities.[7] Laser welding with its inherently small heat affected zone has been considered as a potential solution to these difficulties. A study[8] on the welding and cutting of Inconel 718 with a 15kW CW laser indicated that it could be an effective joining method although there were some isolated instances of microfissuring. Additional studies[9,10] using YAG lasers produced cracks in the nailhead which were attributed to solidification cracking. More recently, pulsed CO_2 laser welding has been applied to wrought Inconel 718 with excellent success in eliminating the microfissures.[11]

III. Material characterization

To better understand the response of the IN 718 structures that were to be welded, Differential Scanning Calorimetry (DSC) was applied to the wrought, grain grown wrought (1 hr. at 1177° C, air cool), and cast. The DSC tests were conducted in argon on 150-160mg samples at two heating and cooling rates. Typical curves for the 40° C/min rate are shown in Figures 3, 4, and 5. The temperatures at which transformations occurred are identified in Table 1 for the three material states being studied. Figure 6 shows the relationship of the transformations (40° C/min runs) with the regions of phase formation for IN 718.[12]

After determining the temperatures for the phase transformations via DSC, high temperature x-ray analysis was conducted to aid in the eventual identification of the phase structures. The data was obtained first at room temperature by scanning through 20° to 120° for 20 angle at 1°/min. The data was collected for each sample state at discrete temperatures (wrought: 540, 570, 600, 730, and 760° C, wrought grain grown: 590, 630, 730, 770, 800° C, and cast: 530, 580, 620, 720, 770, and 820° C). A slow rate of scanning (0.5°/min) was selected for high temperature diffractometry to ensure the detection of slow as well as secondary transformations. In order to avoid the surface oxidation effect on the data, the experiments were conducted in an argon atmosphere. Following the runs, the room temperature x-ray scans were again run on the same samples. Figure 7 shows the x-ray data obtained over these temperatures. Similar analyses are presently being conducted on the fusion zones and heat affected zones of welded samples.

IV. Description of laser and worktable

Bead-on-plate welds were made using a Rofin-Sinar RS3000 fast axial flow CO_2 laser which produces a peak power of 3,700 watts. The laser is radio-frequency excited at 27.12 MHz and is configured to give a TEM_{10} beam mode which has a spatial power distribution described as a ring with a central peak. The wavelength of the beam is 10.6 microns (far-infrared).

Restrained welds were made using a fixture designed specifically for this project. The fixture, in the welding position, is shown in Figure 8. Sample restraint was provided by a pair of jaws that produced both horizontal and vertical pressure on the material (see Figure 9). A slot in the base accommodated the weld underbead. The fixture was mounted on a numerically controlled Aerotech work table which moved the material horizontally beneath the beam.

The beam was focused on the workpiece with an off-axis parabolic mirror having a focal length of 150 mm, equivalent to an f/6 system. The focused laser beam is directed perpendicular to the workpiece through a conical gas flow nozzle. The nozzle delivers a coaxial flow of inert gas which serves to shield the weld while it solidifies and to protect the laser optics from weld spatter. Helium was used as a shielding gas because of its high ionization potential and plasma suppression capabilities. The coaxial gas flow rate was 26 liters/min.

A nozzle positioned to the side of the beam delivery nozzle directed an additional flow of helium towards the workpiece at an angle of 45 degrees from the vertical and thus served as a separate means of plasma control. The plasma control gas flow rate was 20 liters/min.

A. Pulsing and delivered power

The laser output can be continuous-wave (CW) or pulsed. The pulsing format chosen for this experiment was the mixed frequency format (5 kHz pulse width modulation on/gated pulse on) shown in Figure 10.

When the laser is operated in the mixed frequency pulse format the output is gated into pulses with a frequency which is set by independent adjustments of the time on and time off for one pulse cycle. In addition, each gated pulse is composed of multiple high frequency (5 kHz) pulses. The 5 kHz duty cycle is ad-

justable (pulse width modulation) such that the power delivered during the time on of each gated pulse (pulse average power) is adjustable from 7 to 100 percent of peak power (260 to 3,700 watts).

The duty cycle of the low frequency gated pulses is defined as the time on divided by the total time for one pulse cycle. Therefore, the average power delivered during welding is equal to the duty cycle multiplied by the pulse average power.

Welds were attempted using the lowest specific energy input (energy per unit length of weld) possible in an effort to increase the cooling rate, reduce the heat affected zone width, and decrease the incidence of microfissures while maintaining full penetration. Pulse tailoring using the mixed frequency pulse format afforded the greatest flexibility in the selection of welding parameters with lower specific energies than those obtainable with continuous welding processes.

B. General procedure

Prior to the experiment the delivered power was measured using a Scientech water cooled calorimeter. The results are shown in Figure 11. The delivered power is slightly less than the laser controls indicate because of losses in the beam delivery and focussing system. Because the losses were minimal, the laser control indicator was used for subsequent power settings.

The focal position was determined by quickly passing a plexiglass specimen, held on a special fixture, through the beam at an angle of 6 degrees from vertical. Seven measurements were made at different powers. A hyperbolic impression was burned into the plexiglass, and the narrowest point in the impression was considered to be the focal point of the laser beam.

The distance from the bottom (datum) edge on the plexiglass to the narrowest point in the impression was measured using a 20X optical comparator. The distance from a known datum on the laser weld head to the bottom of the plexiglass was measured using the positional outputs from the CNC motion system. The focal position was then determined by subtracting the plexiglass datum to focal impression distance from the weld head datum to plexiglass datum distance. The focal position location did not appear to be functionally related to the laser power, and a mean value of the seven measurements was used as a determination of focal position.

Previous Inconel welds at UTSI were produced with the beam focused at 3 mm below the plane of the top surface. To determine the optimum focal position for the present research, unrestrained bead-on-plate welds were produced at focal positions from 1 to 4 mm below the sample surface. The best penetration for the 3.2 mm thick material was produced when the focus was from 2 to 3 mm below the surface. A focal position of 3 mm below the surface was maintained in order to be consistent with the previous work.[11]

The following parameters were kept fixed for all experiments:

1. Beam mode (TEM_{10});
2. Focussing system (f/6 off-axis parabola);
3. Focus position (3 mm below workpiece surface);
4. Pulse format (mixed frequency);
5. Nozzle standoff distance (6 mm);
6. Coaxial gas (helium, 26 liters/min);
7. Side gas jet (helium, 20 liters/min).

Four experiment matrices were selected for this study. They are: unrestrained weld matrix, restrained weld matrix, variable duty cycle weld matrix, and pedigree weld matrix. These are discussed in detail in the following sections.

C. Unrestrained weld matrix

During the first phase of the experiment, unrestrained bead-on-plate welds were produced on 1/8-inch (3.2 mm) wrought Inconel 718. Pulse average power, pulse duty cycle, and weld translation speed were the welding parameters that were varied in order to find a matrix of weld parameters which met the penetration criterion. This criterion was established as a continuous underbead with a minimum width between 0.8 and 0.9 mm. The function of the penetration criterion was to give the researchers a measurable standard by which to compare welds produced with different welding parameters.

After processing, the weld underbead was measured with a scaled loop (Magnification: 10 X, Scale Divisions: one-tenth of a millimeter). For welds which did not meet the penetration criterion, the pulse average power was either increased or decreased while the pulse duty cycle and translation velocity were held constant. In this manner the parameters which give acceptable penetration were determined. The final weld conditions are given in Table 2. A "U" precedes the sample number to designate the weld as unrestrained.

During the welding just described, it was observed that welds produced at the lowest duty cycles could be made to meet the penetration criterion over a wider range of pulse average powers than could the high duty cycle welds. Weld conditions U28, U29, U30, U31, and U32 were selected for further examination of this

behavior because they spanned a range of duty cycles from 37 to 71 percent at the same translation velocity.

These five conditions were rewelded, and this time the pulse power was increased until excessive penetration (minimum underbead width greater than 0.9 mm) was observed. The welds were again made and the pulse power lowered until under penetration was achieved (minimum underbead width less than 0.8 mm).

D. Restrained weld matrix

Restrained weld samples were cut to 3.5 cm by 0.95 cm from the as-received stock of thickness 3.2 mm (1/8-inch). Paint and oil were removed from the surface with an acetone flush.

The samples were clamped into the fixture (Figure 9) by first tightening the four vertical jaw bolts until they contacted their seating surfaces, preventing vertical jaw movements. Next, the two horizontal jaw bolts were hand-tightened, thus applying pressure horizontally. The vertical jaw bolts were further tightened, thus applying downward pressure. After the samples were welded, they were left in the fixture until the sample was cool to the touch and the tightening procedure was reversed.

Restrained welds were performed at five duty cycles (37, 52, 61, 71, and 80 percent), four pulse average power levels (2600, 2250, 2050, and 1900 watts), and a translation velocity of 12 mm/s; twenty conditions were used to produce the samples. Four fully penetrated conditions were repeated from the unrestrained matrix. These were U28, U29, U30, and U31.

The restrained weld conditions were selected so that the effect of duty cycle and/or the effect of pulse average power on the weld microstructure (microfissures and porosity) could be examined along lines of constant duty cycle (with changes in pulse average power) or along lines of constant pulse average power (with changes in duty cycle). In this manner a matrix of conditions (Table 3) was established. An "R" precedes the sample number to designate a restrained weld.

E. Variable duty cycle weld matrix

The purpose of this experiment was to investigate the microstructural relationship between pulsed laser welds in small grain wrought (ASTM #8 or smaller), grain grown wrought (ASTM #5), and cast (ASTM #2) Inconel 718. Restrained bead-on-plate welds were carried out using the same welding fixture and restraint as used in the restrained weld matrix.

The small grain wrought and grain grown wrought samples were cut from sheet stock while the cast samples were cut from a cast bar using an abrasive cut-off saw. The thickness for all samples was 1/8-inch (3.2 mm). All samples were cleaned with acetone immediately prior to welding.

The translation speed was kept constant at 12 mm/s and the pulse average power was also kept constant at 2250 W. Weld duty cycle was the experimental variable and the values used are shown in Table 4. The designation RW indicates that these samples were wrought Inconel 718 welded in the restrained condition. Likewise, RG indicates restrained welds on grain grown material, and RC indicates restrained welds on cast material.

F. Pedigree weld matrix

The purpose of the pedigree weld matrix was to demonstrate that three welds from the restrained matrix, which were free from microfissures and porosity, could be reproduced with a quantitative level of confidence. The conditions for the pedigree matrix are listed in Table 5. Along with being free from microfissures and porosity, these conditions are near the median of pulse average power, and near the median of the duty cycles used for the restrained matrix.

The samples were cut to the standard size (3.5 × 0.95 cm), cleaned, and placed in the welding fixture in the same manner as the restrained matrix samples. After welding, the samples were left in the fixture until they were cool to the touch. Nine samples (three for each condition) were welded.

G. Metallographic analysis of samples

The restrained weld matrix, pedigree weld matrix, and variable duty cycle weld matrix samples were transversely cut to begin the metallurgical analysis. Longitudinal sections of selected restrained weld samples were ground with a surface grinder in 0.2 mm increments parallel to the surface. Part of each variable duty cycle specimen was slant-ground using the technique shown in Figure 12. All sections were mounted in thermosetting mounting material and then ground with silicon-carbide abrasive paper. Paper of 80, 120, 180, 240, 320, 400, and 600 grit was used in succession for grinding. The samples were then polished with 6-micron diamond paste on a cloth wheel to remove visible scratches.

Immediately after the samples were polished they were etched with Waterless Kallings reagent to reveal the microstructure. The reagent was applied with a cotton swab and left on for about 15 seconds or until the weld was clearly visible. The samples were

rinsed in running water, then ultrasonically cleaned in distilled water and air dried to remove the remaining reagent. An Olympus Model PME inverted-stage metallurgical microscope was used at magnifications from 13X to 1000X to examine and photograph the transverse cross sections.

Images of the longitudinal restrained matrix weld sections were obtained with a video camera and macrolens attached to a Vicom digital image processor. The outline of the longitudinal section was traced, and the area and perimeter enclosed by the trace were calculated by the Vicom. Longitudinal curvature was calculated by dividing the perimeter by the enclosed area. Since the welds have a three dimensional structure dependent on duty cycle, measurements of the longitudinal and transverse curvature were made as a basis for comparison between welds.

In order to calculate the transverse curvature, the outlines of the weld from the first, third, fifth, and seventh cross sections were stacked together in one image and the resulting contour map was photographed. The spacing between the lines on the contour map was measured at ten stations spaced every 3.5 mm. This spacing was selected because the measurements spanned the length welded by two pulses of the condition having the greatest pulse spacing (duty cycle of 37 percent, pulse average power of 2050 watts).

The method for establishing an approximate transverse cross sectional shape at an individual station is depicted for a typical weld in Figure 13. Transverse curvature is calculated by dividing the perimeter of the transverse cross section by the area (sum of areas A, B, and C).

In practice, most of the microfissures that are observed after welding this material are found in the heat affected zone (HAZ) beneath the weld nailhead. Microhardness measurements to determine HAZ width were made on samples U9, U28 and an unrestrained CW weld using a Buehler Micromet II hardness tester with 500 gram mass impact. The impact time was set at 15 seconds.

V. Results

A. Unrestrained welds

Unrestrained bead-on-plate welds were produced on 1/8-inch thick wrought Inconel 718. The process parameters (pulse average power, pulse duty cycle, and weld translation velocity) were varied in order to find a matrix of weld parameters which met penetration and continuous underbead criteria.

1. Relationships between weld parameters

Unrestrained, fully penetrated welds (0.8 to 0.9 mm minimum underbead width) were produced over a wide range of pulse duty cycles, pulse average powers, and weld translation velocities. As seen in Figure 14, a near-linear relationship exists between the pulse average power and the pulse duty cycle required to produce full penetration for a given weld translation velocity.

Penetration measurements also revealed a dependence of the acceptable pulse average power range on duty cycle (Figure 15). For example, sample U31 (37 percent duty cycle, 2600 W, 12 mm/s) had a range of 700 watts, while sample U28 (71 percent duty cycle, 1900 W, 12 mm/s) had only a 100 watt range between overpenetration and underpenetration. Therefore, the low duty cycle welds were more tolerant to pulse average power variations.

2. Centerline cracks

Large centerline cracks were observed in some unrestrained welds. These were thought to occur because the small samples had no surrounding unaffected material to provide restraint during weld pool melting and resolidification. Figure 16 shows that fully penetrated welds having a duty cycle less than 54 percent exhibited no centerline cracks regardless of changes in the other weld parameters (pulse average power, speed). This indicates that the long off-times that are characteristic of low duty cycle welds give sufficient time for the weld to solidify and strengthen before additional heat from a subsequent pulse is added. Low duty cycle welds are therefore less prone to centerline cracking when mechanical restraint is not provided.

3. Heat affected zone width

Microhardness measurements across the weld and into the matrix metal (Figures 17, 18 and 19) were used to determine the width of the heat affected zone (HAZ). Material which had no increase in hardness above that of the matrix was presumed to be outside of the HAZ. Weld condition U9 (61 percent duty cycle) had a heat affected zone width averaging 48 percent of the weld width, whereas weld condition U28 (71 percent duty cycle) had a heat affected zone width averaging 65 percent of weld width. In comparison, the HAZ of a similar (unrestrained) CW weld (2500 W, 1.5 M/min) on the same material was 61 percent of weld width. The results indicate that a weld having a duty cycle of 71 percent or more has a HAZ width that is approximately equal to the HAZ width of a CW weld.

B. Restrained welds

The unaffected material surrounding a weld acts as restraint during solidification. The small sample size used for this experiment necessitated the use of mechanical restraint since there was a limited amount of unaffected material surrounding the weld.

1. Nailhead microfissures

Figures 20, 21, and 22 show typical weld cross sections. Figures 23, 24, and 25 show typical weld microstructures at increasing magnifications. Although precipitates have accumulated in the grain boundaries within the heat affected zone beneath the nailhead, nailhead microfissures were not observed in any of the restrained weld cross sections.

The absence of cracking in the restrained welds produced by the laser for this study may be attributed to the rapid cooling rate and its associated small heat affected zone and limited extent of grain boundary liquation. In addition, the low total heat input to the welds, which is made possible by the use of pulse tailored laser welding, lessens the localized strains which occur in the HAZ.

2. Porosity

Restrained welds having large centerline pores are indicated on Figure 26 along with the other welds in that matrix. Pores were more likely to occur in welds which were processed with the lowest duty cycles and/or the lowest pulse average powers. During the "beam-off" portion of the pulsing cycle, the internal pressure in the keyhole decreases to the point that it will no longer support the walls and the keyhole partially collapses. Keyhole gases (metallic plasma), trapped by the collapsing of the keyhole, can nucleate into spherical pores which are engulfed by the rapid solidification front before they rise to the surface. These gases would then condense and solidify as the weld cools, leaving a void.

The high duty cycle and high pulse power welds did not exhibit porosity. The higher specific energy inputs significantly increase the time that the weld pool remains molten, thus allowing any pores which have nucleated the time to escape the molten material.

3. Nailhead curvature

Longitudinal curvature was calculated by dividing the perimeter of the longitudinal section by the longitudinal area. The results are found in Tables 6 and 7. Transverse curvature was calculated from cross sections obtained using the technique shown in Figure 13. Table 8 lists the mean value of ten measurements for each weld. The results must be regarded as approximate since the assumption of linearity between contours was made; the errors should be small since the difference in depth between contours is small.

It is desirable to reduce the two curvature values for each weld to a single curvature rating in order to compare the welds within the matrix. The individual values were first normalized by expressing them as a fraction of the largest value obtained by the same method.

It was assumed that the transverse and longitudinal curvature were equally important and therefore given equal weight. The curvature rating was calculated as the sum of the normalized longitudinal and transverse curvatures. As seen in Table 9, the curvature rating is inversely related to duty cycle and pulse average power.

C. Variable duty cycle weld matrix

Figure 2 shows the base material microstructures that were used in this study. The wrought grain grown (ASTM #5) has significantly larger grains than the wrought (ASTM #8). It also exhibits fewer transformation regions during DSC analysis, a result of the recovery and solutionizing which occurs during the grain growth treatment. The cast structure is large grained (ASTM #2) and obviously dendritic with extensive segregation. DSC analysis shows similar transformations to the wrought and wrought grain grown but with a significant transformation occurring around 1180° C which is probably incipient melting as a result of the segregation.

Subsequent to welding, the three Alloy 718 materials exhibited precipitation and evidence of grain boundary liquation and interdendritic remelting in the heat affected zones. Figure 27, 28 and 29 show microstructures in the region of the nailhead. The visually affected region extends 0.098±0.015 mm from the fusion zone in the wrought material, 0.139±0.001 mm from the fusion zone in the wrought grain grown material, and 0.309±0.147 mm from the fusion zone in the cast material.

D. Pedigree welding trials

Five metallurgical cross-sections were prepared from each of the nine samples welded using the conditions shown in Table 4. The cross-sections were examined at 100X magnification. Although some grain boundary precipitation was observed in the region adjacent to the nailhead, no microfissures and porosity were found. The cross-sections were then crack tested using the dye-penetrant technique. No cracks were detected.

Acknowledgments

The authors would like to acknowledge the contributions of the Marshall Space Flight Center, Materials and Processes Laboratory and in particular Mr. R. J. Schwinghamer and Mr. Ernie Bayless for providing the wrought Inconel. The High Temperature Materials Laboratory at Oak Ridge National Laboratory allowed access to their Differential Scanning Calorimeter and their high temperature x-ray diffractometer through their user program. Discussions and collaboration with ORNL personnel through this program have been invaluable. In particular the authors would like to thank the Center for Advanced Space Propulsion for their sponsorship of this work. This work was performed within the Center for Advanced Space Propulsion and was supported in part by NASA Grant No. NAGW-1195. The Center for Advanced Space Propulsion is part of the UT- Calspan Center for Aerospace Research, a not-for-profit organization located at UTSI.

References

1. John R. Radavich, "Metallography of Alloy 718," Journal of Metals, July 1988, pp. 42-43.
2. C. T. Sims, N. S. Stoloff and W. C. Hagel, **Superalloys II**, John Wiley and Sons, New York (1987).
   John R. Radavich, "The Physical Metallurgy of Cast and Wrought Alloy 718," **Superalloy 718 - Metallurgy and Applications**, ed. E.A. Loria, The Minerals, Metals and Materials Society, pp. 229-240, 1989.
3. R. Cozar and A. Pineau, Met. Trans. 4, 47 (1973).
4. H. L. Eiselstein, "Advances in the Technology of Stainless Steels and Related Alloys," STP 369, ASTM Philadelphia, PA, pp. 62-67, 1965.
5. W. J. Boesch and H. B. Canada, J. Met., 21 (10), 34 (1969).
6. T. J. Kelly, "Investigation of Elemental Effects on the Weldability of Cast Nickel-Based Superalloys," **Advances in Welding Science and Technology TWR '86**, ed. S. A. David (May 1986) pp. 623-627.
7. R. G. Thompson, "Microfissuring of Alloy 718 in the Weld Heat-Affected Zone," Journal of Metals, July 1988, pp. 44-48.
8. C. M. Banas, Final Report, Contract NAS8-36306.
9. L. A. Weeter, C. E. Albright and W. H. Jones, Welding Research Supplement, March 1986, 51s-62s.
10. J. P. Reynolds, H. W. Kerr, P. J. Fenrenbach, L. Bourque, and R. D. Davidson, **Advances in Welding Science and Technology, TWR '86**, Proceedings of an International Conference on Trends in Welding Research, May 1986, Ed. S. A. David, ASM International.
11. M. Sharp, M. H. McCay, T. D. McCay, N. B. Dahotre, A. Sedghinasab and S. Gopinathan, "Pulsed Laser Welding of Inco 718," **ICALEO '89 Proceedings**, Volume 69, Laser Material Processing, October 1989, pp. 229-238.
12. R. G. Carlson and J. F. Radavich, "Microstructural Characterization of CAST 718," Superalloy 718 - Metallurgy and Applications, ed. E. A. Loria, The Minerals, Metals & Materials Society, 1989, pp. 79-95.

Table 1. Transformation Temperatures in IN 718.

Sample	DSC Treatment	Transformation Temperatures (° C)
Wrought	Heating 10°C/min	568, 702, 1030, 1220, 1280
	Cooling 10°C/min	760, 1270
	Heating 40°C/min	615, 760, 912, 1025, 1220, 1275
	Cooling 40°C/min	730, 1100, 1150, 1265
Wrought Grain Grown	Heating 10°C/min	592, 775, 1230, 1280
	Cooling 10°C/min	765, 1272
	Heating 40°C/min	655, 850, 1220
	Cooling 40°C/min	1100, 1266
Cast	Heating 10°C/min	538, 725, 1175
	Cooling 10°C/min	1265
	Heating 40°C/min	585, 770, 1130, 1180, 1205, 1280
	Cooling 40°C/min	1160, 1267

Table 2. Unrestrained Weld Matrix.

Designation	Translation Velocity (mm/s)	Pulse Average Power (W)	On Time (ms)	Off Time (ms)	Duty Cycle (%)	Specific Energy (J/mm)	Underbead Width (mm)
U1	25	2500	17	3	85	85.0	1.0
U2	25	3000	17	7	71	85.2	1.0
U3	25	3000	17	21	45	54.0	0.6
U4	25	2700	17	7	71	76.7	0.8
U5	25	2900	17	11	61	70.7	0.8
U6	25	2475	17	4	81	80.2	0.8
U7	18	2000	23	4	85	94.4	0.6
U8	18	2333	22	9	71	92.0	0.8
U9	18	2567	23	15	61	87.0	0.8
U10	18	2857	24	21	53	84.1	0.9
U11	18	2125	22	6	79	93.3	0.9
U12	18	3000	22	33	40	66.7	0.8
U13	18	2775	22	22	50	77.1	0.8
U14	15	1900	28	5	85	107.7	1.0
U15	15	2150	29	12	71	101.8	1.0
U16	15	2150	28	18	61	87.4	0.8
U17	15	2600	28	25	53	91.9	1.0
U18	15	2500	28	24	54	90.0	1.2
U19	15	2650	28	33	46	81.3	0.9
U20	15	3000	28	76	27	54.0	0.0
U21	15	2530	28	28	50	84.3	0.8
U22	15	2200	28	42	40	58.7	0.0
U23	15	2000	28	7	80	106.7	0.8
U24	15	2725	28	42	40	72.7	0.9
U25	15	2250	28	19	60	90.0	0.8
U26	15	2125	28	12	70	99.2	1.0
U27	12	1850	34	6	85	131.0	1.0
U28	12	1900	36	15	71	112.4	0.9
U29	12	2050	36	23	61	104.2	0.8
U30	12	2250	35	32	52	97.5	0.9
U31	12	2600	35	60	37	80.2	0.8
U32	12	2400	35	43	45	90.0	0.8
U33	12	3000	35	198	15	37.5	0.0
U34	12	2400	35	42	45	90.0	0.8

Table 3. Restrained Weld Matrix, Translation Velocity = 12 min/s.

Designation	Pulse Average Power (W)	On Time (ms)	Off Time (ms)	Duty Cycle (%)	Specific Energy (J/mm)
R1	1900	36	9	80	127
R2	1900	36	15	71	112
R3	1900	36	23	61	97
R4	1900	35	32	52	83
R5	1900	35	60	37	58
R6	2050	36	9	80	137
R7	2050	36	15	71	121
R8	2050	36	23	61	104
R9	2050	35	32	52	89
R10	2050	35	60	37	63
R11	2250	36	9	80	150
R12	2250	36	15	71	132
R13	2250	36	23	61	114
R14	2250	35	32	52	98
R15	2250	35	60	37	69
R16	2600	36	9	80	173
R17	2600	36	15	71	153
R18	2600	36	23	61	132
R19	2600	35	32	52	113
R20	2600	35	60	37	80

Table 4. Variable Duty Cycle Weld Matrix, Translation Velocity = 12 min/s.

Designation	Pulse Average Power (W)	On Time (ms)	Off Time (ms)	Duty Cycle (%)	Specific Energy (J/mm)
RW1	2250	35	60	35	69.4
RW2	2250	35	32	52	97.5
RW3	2250	36	23	61	114.4
RW4	2250	36	15	71	133.1
RW5	2250	36	9	80	150.0
RW6	2250	36	4	90	168.8
RW7	2250	-	-	CW	187.5
RG1	2250	35	60	35	69.4
RG2	2250	35	32	52	97.5
RG3	2250	36	23	61	114.4
RG4	2250	36	15	71	133.1
RG5	2250	36	9	80	150.0
RG6	2250	36	4	90	168.8
RG7	2250	-	-	CW	187.5
RC1	2250	35	60	35	69.4
RC2	2250	35	32	52	97.5
RC3	2250	36	23	61	114.4
RC4	2250	36	15	71	133.1
RC5	2250	36	9	80	150.0
RC6	2250	36	4	90	168.8
RC7	2250	-	-	CW	187.5

Table 5. Pedigree Weld Matrix, Translation Velocity = 12 min/s.

Designation	Pulse Average Power (W)	On Time (ms)	Off Time (ms)	Duty Cycle (%)	Specific Energy (J/mm)
P1	2600	36	23	61	132
P2	2250	36	23	61	114
P3	1900	36	15	71	112

Table 6. Longitudinal Curvature Data for Restrained 61 Percent Duty Cycle Welds.

Sample	Depth (mm)	Perimeter (mm)	Area (sq. mm)	Curvature (1/mm)
R3	0.20	28.152	23.296	1.208
	0.38	26.916	20.759	1.297
	0.53	26.568	18.491	1.437
	0.66	26.452	16.137	1.639
	0.81	28.113	15.314	1.836
	1.04	27.186	14.877	1.827
	1.37	27.070	15.432	1.754
R8	0.20	28.036	22.310	1.257
	0.41	26.723	20.952	1.275
	0.53	27.070	19.221	1.408
	0.66	26.337	17.725	1.486
	0.84	28.152	16.240	1.733
	1.07	25.719	14.540	1.769
	1.37	26.259	15.528	1.691
R13	0.20	26.568	23.427	1.134
	0.41	28.229	23.860	1.183
	0.53	27.070	22.096	1.225
	0.69	27.109	20.696	1.310
	0.86	27.186	18.950	1.435
	1.07	25.873	16.113	1.606
	1.40	26.877	16.040	1.676
R18	0.20	28.113	27.164	1.035
	0.38	27.881	27.013	1.032
	0.51	27.611	25.611	1.078
	0.69	26.877	24.380	1.102
	0.86	27.070	23.548	1.150
	1.04	26.646	20.108	1.325
	1.35	28.152	18.896	1.490

Table 7. Longitudinal Curvature Data for Restrained 2050 Watt Pulse Average Power Welds.

Sample	Depth (mm)	Perimeter (mm)	Area (sq. mm)	Curvature (1/mm)
R6	0.00	26.852	26.573	1.010
	0.23	28.547	28.193	1.013
	0.51	29.047	27.657	1.050
	0.66	28.046	25.368	1.106
	0.94	27.853	22.651	1.230
	1.14	27.006	20.876	1.294
	1.30	26.813	20.030	1.339
R7	0.00	28.624	23.035	1.243
	0.33	29.394	24.765	1.187
	0.61	28.084	22.445	1.251
	0.79	27.352	20.966	1.305
	0.99	27.006	18.855	1.432
	1.19	26.543	16.354	1.623
	1.37	26.890	15.802	1.702
R8	0.20	28.036	22.310	1.257
	0.41	26.723	20.952	1.275
	0.53	27.070	19.221	1.408
	0.66	26.337	17.725	1.486
	0.84	28.152	16.240	1.733
	1.07	25.719	14.540	1.769
	1.37	26.259	15.528	1.691
R9	0.00	28.277	23.291	1.214
	0.28	27.468	22.642	1.213
	0.51	27.661	20.020	1.382
	0.79	26.813	16.544	1.621
	0.94	27.314	15.090	1.810
	1.14	25.773	12.978	1.986
	1.32	26.697	13.201	2.022
R10	0.00	29.510	24.160	1.221
	0.28	29.047	23.504	1.236
	0.48	29.202	18.983	1.538
	0.76	27.314	12.780	2.137
	0.94	27.584	12.617	2.186
	1.12	28.316	12.516	2.262
	1.32	28.277	12.647	2.236

Table 8. Transverse Curvature of Restrained Welds.

Sample +	Mean Curvature* (1/mm)	Standard Deviation
R3	0.231	0.005
R8	0.207	0.006
R13	0.215	0.006
R18	0.215	0.008
R6	0.186	0.005
R7	0.204	0.007
R9	0.211	0.006
R10	0.206	0.007

+ Samples R3, R8, R13, and R18 are 61 percent duty cycle welds. Samples R6, R7, R8, R9, and R10 are 2050 watt welds.
* Represents mean values of ten measurement stations per contour plot.

Table 9. Weld Curvature Summary.

Sample	Mean Longitudinal Curvature (Normalized Value)	Mean Transverse Curvature (Normalized Value)	Curvature Rating
R3	1.571 (0.858)	0.231 (1.000)	1.858
R8	1.517 (0.829)	0.207 (0.896)	1.725
R13	1.367 (0.747)	0.215 (0.931)	1.678
R18	1.173 (0.641)	0.215 (0.931)	1.572
R6	1.149 (0.628)	0.186 (0.805)	1.433
R7	1.392 (0.760)	0.204 (0.883)	1.643
R9	1.607 (0.878)	0.211 (0.913)	1.791
R10	1.831 (1.000)	0.206 (0.892)	1.892

Table 10. Weld Metallographic Observations.

Sample	Nailhead Microfissures	Large Pores
R1	N	Y
R2	N	N
R3	N	Y
R4	N	Y
R5	N	Y
R6	N	N
R7	N	N
R8	N	Y
R9	N	Y
R10	N	Y
R11	N	N
R12	N	N
R13	N	N
R14	N	N
R15	N	Y
R16	N	N
R17	N	N
R18	N	N
R19	N	N
R20	N	Y
P1	N	N
P2	N	N
P3	N	N

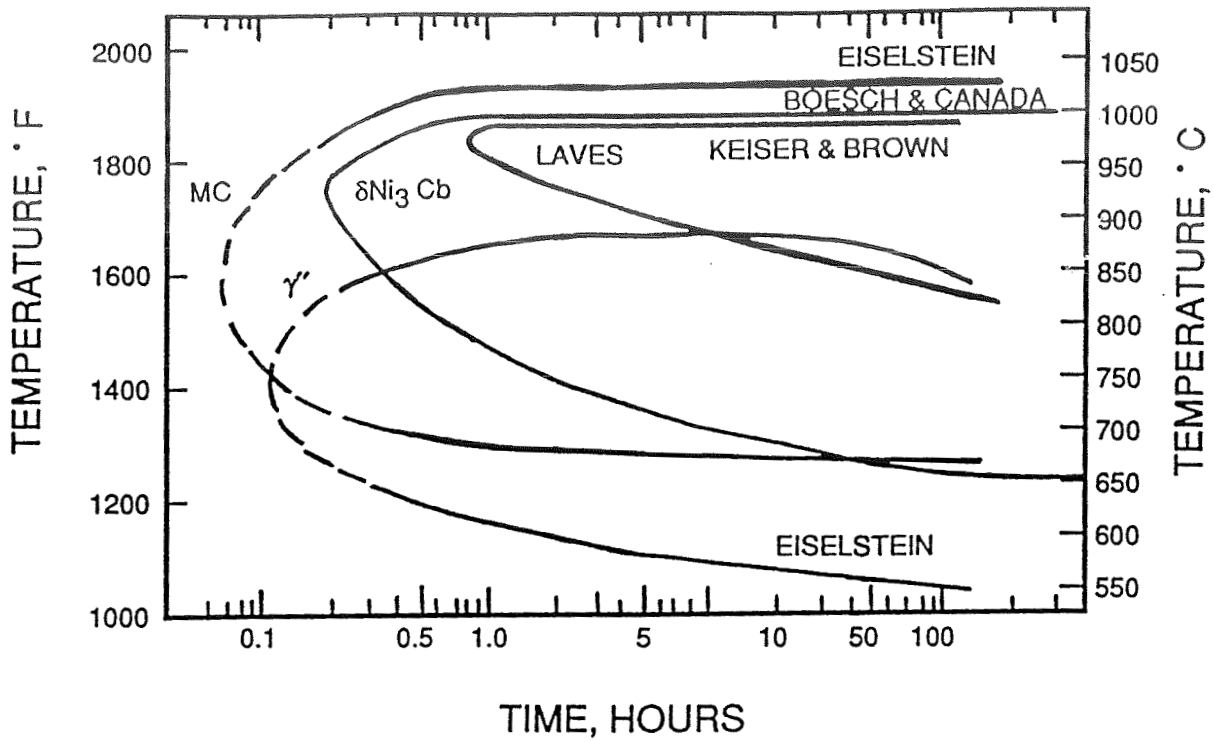

Figure 1. Time-temperature precipitation (TTP) diagrams for Inconel 718 illustrating the kinetics of formation for MC, M_6C, Laves, δ, and γ' phases.[2]

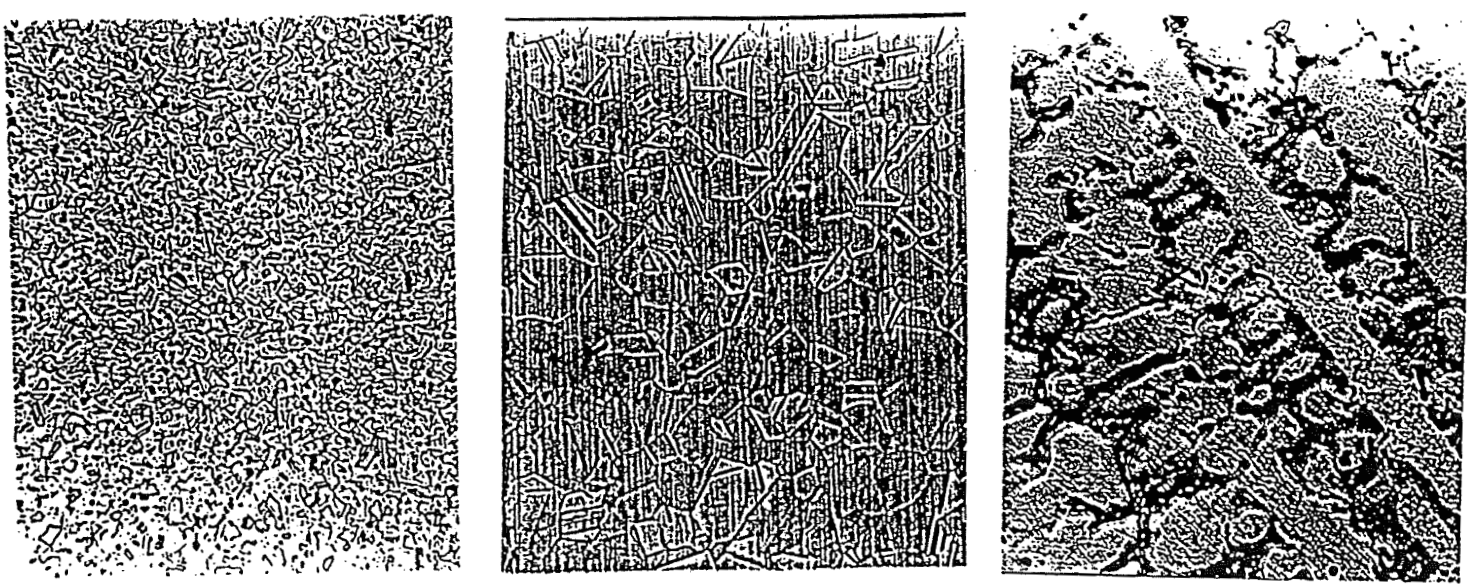

(a) (b) (c)

Figure 2. Typical microstructures, of IN 718 (a) wrought, (b) wrought grain grown, and (c) cast (100X).

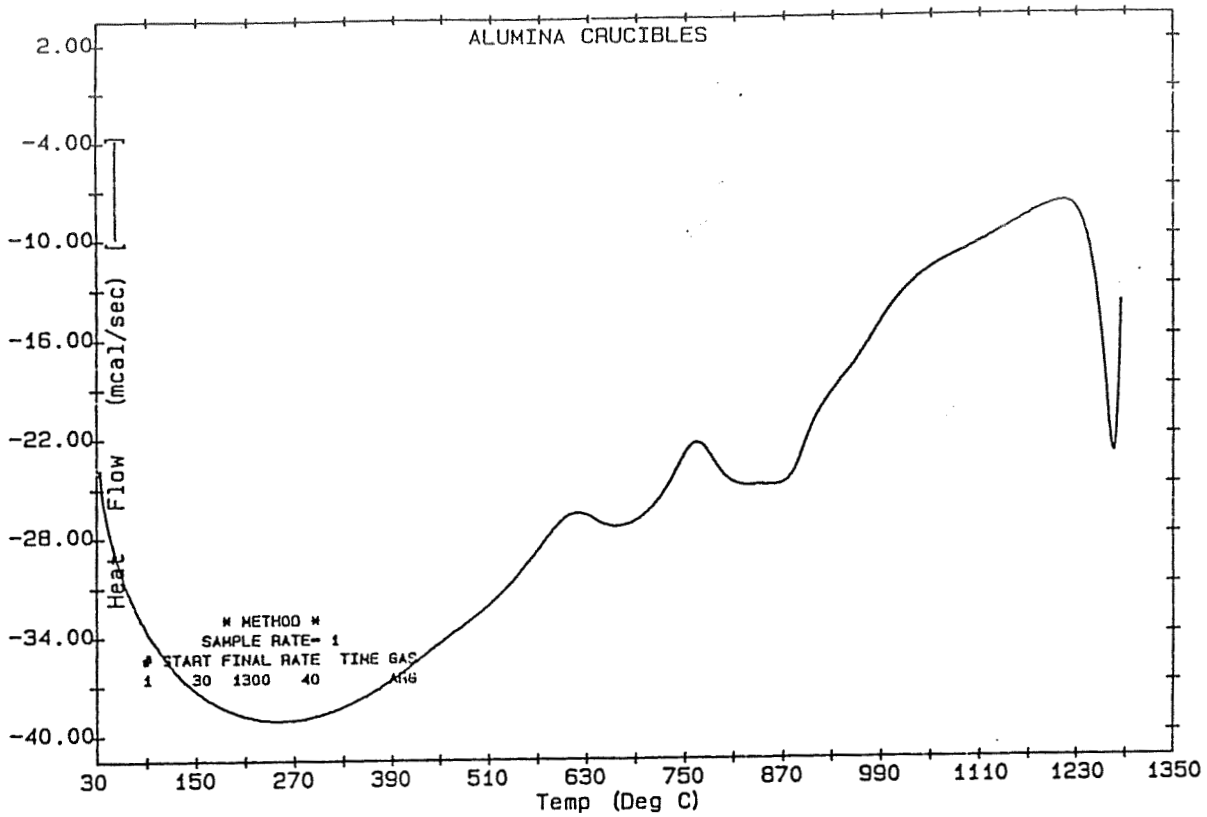

(a)

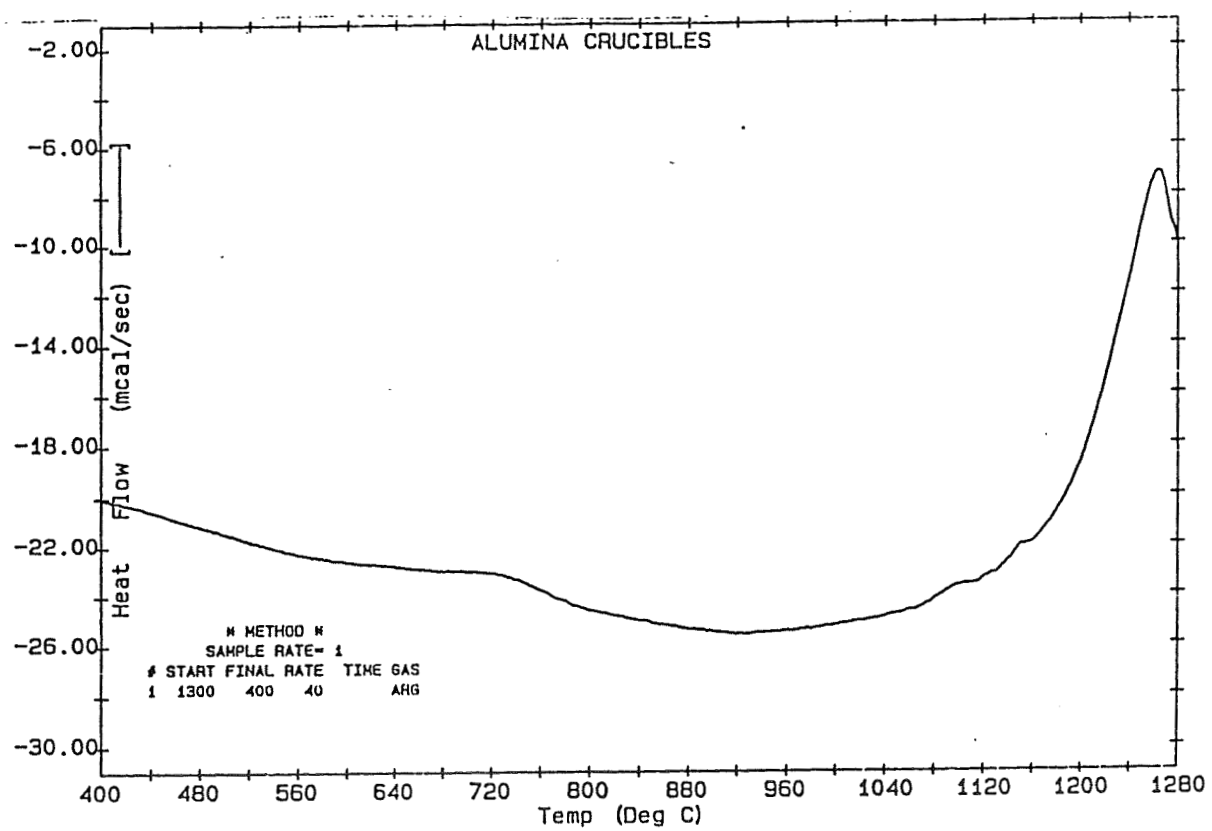

(b)

Figure 3. Differential Scanning Calorimetry curves of wrought IN 718 (a) Heating at 40°C/min, (b) cooling at 40°C/min.

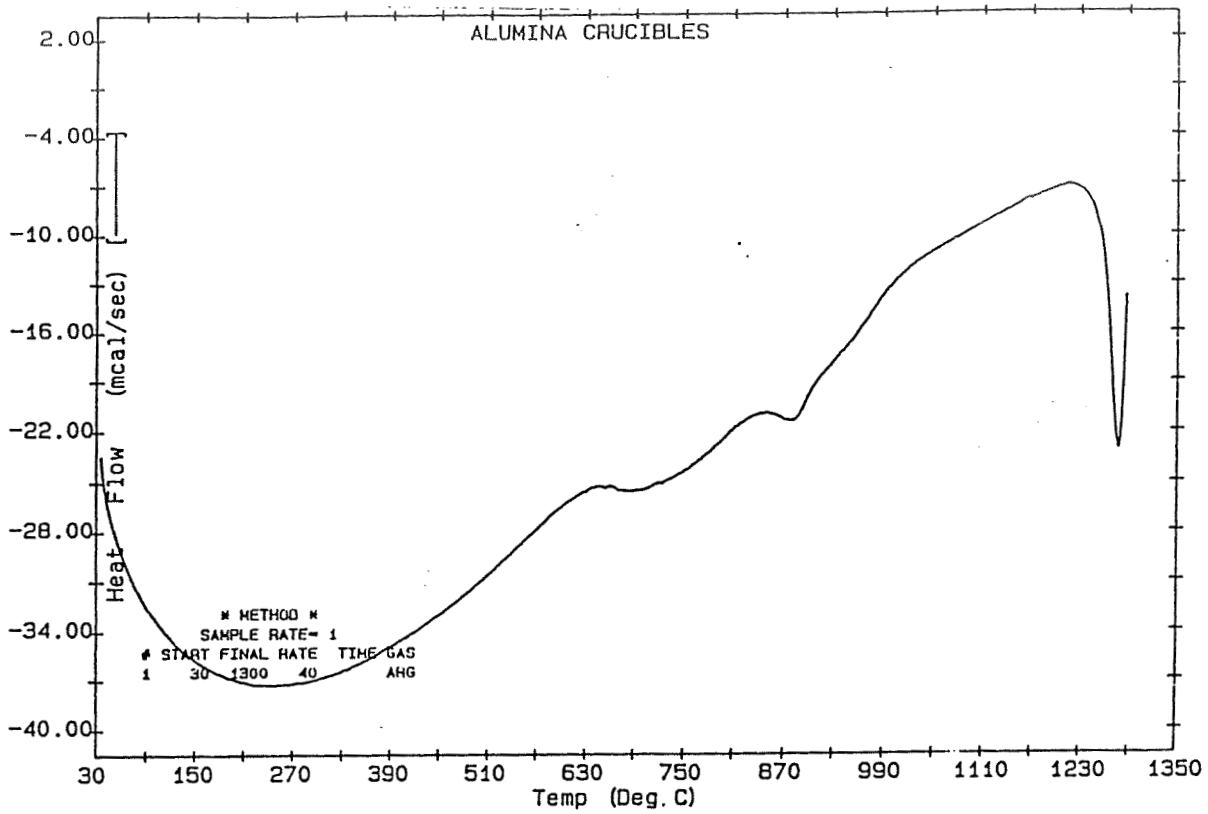

(a)

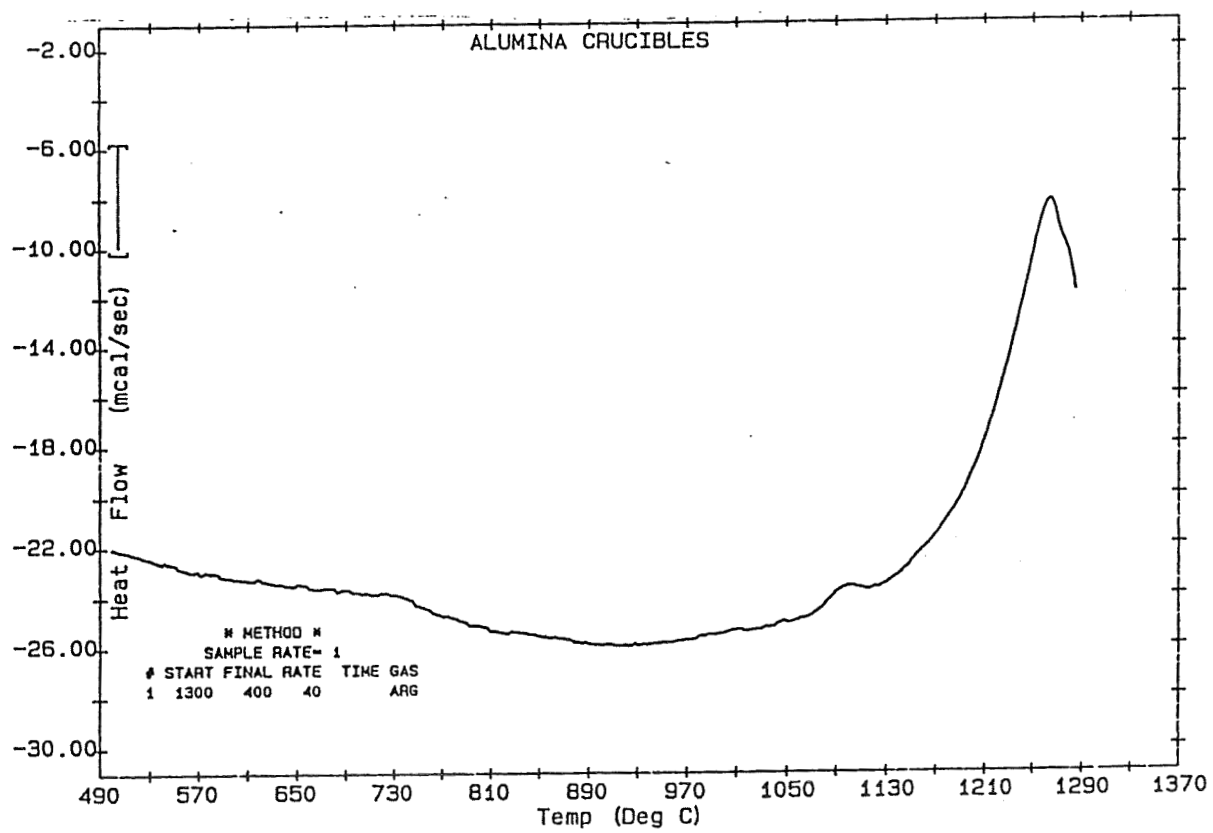

(b)

Figure 4. Differential Scanning Calorimetry curves of wrought grain grown IN 718 (a) Heating at 40°C/min, (b) cooling at 40°C/min.

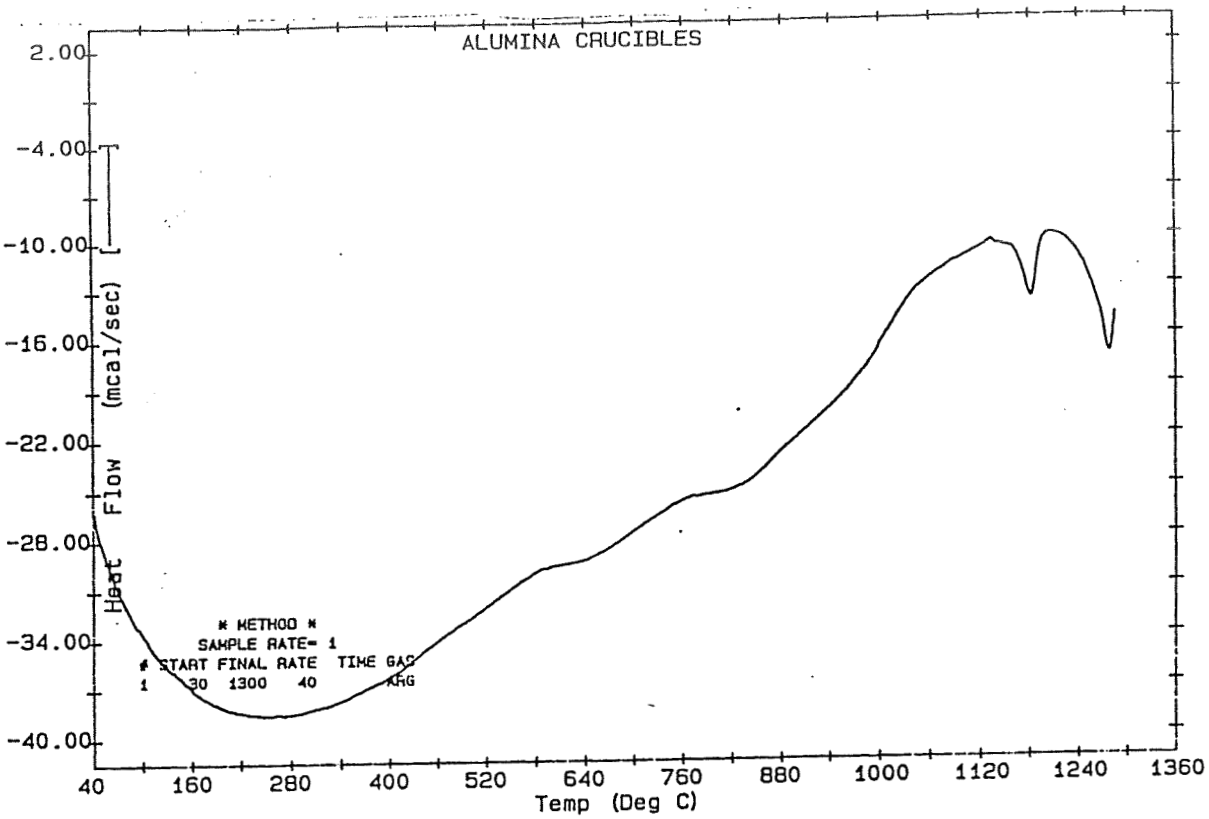

(a)

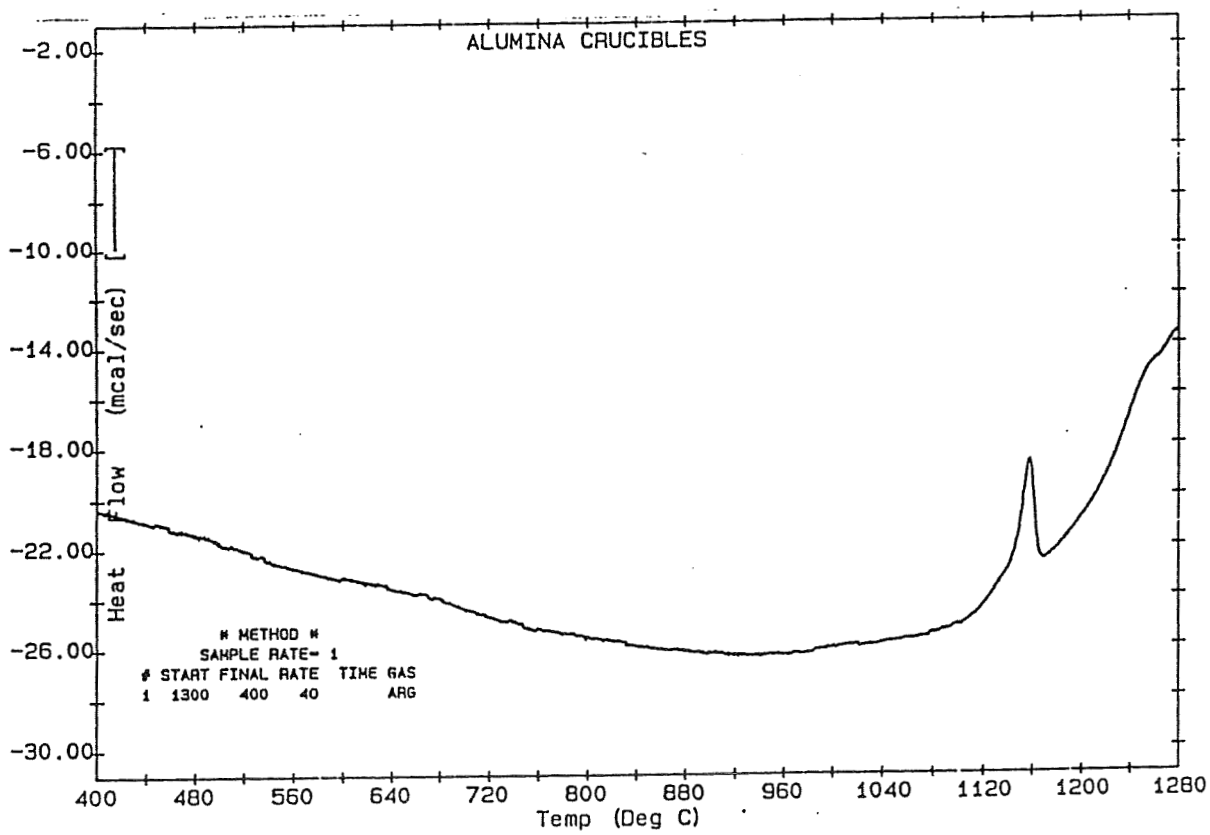

(b)

Figure 5. Differential Scanning Calorimetry curves of cast IN 718 (a) Heating at 40°C/min, (b) cooling at 40°C/min.

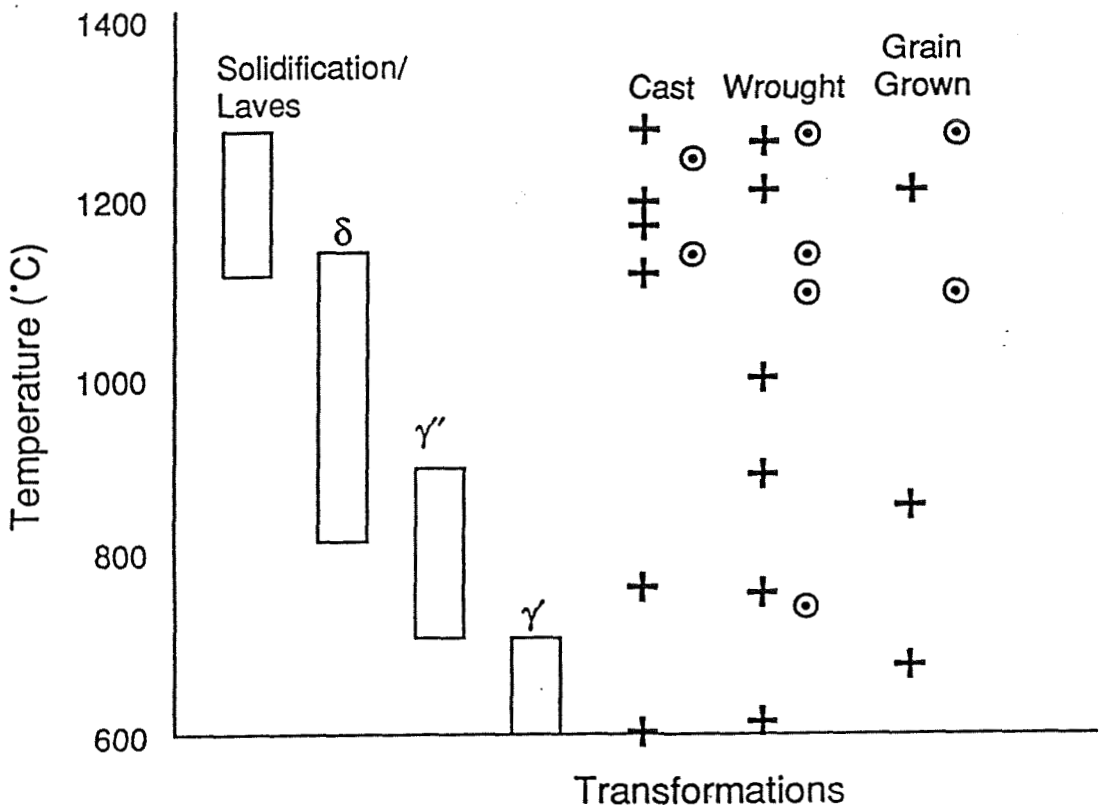

+ Represents DSC identified transformations while heating (40°C/min).
⊙ Represents DSC identified transformations while cooling (40°C/min).

Figure 6. Transformation temperatures for phases in Inconel 718.[2]

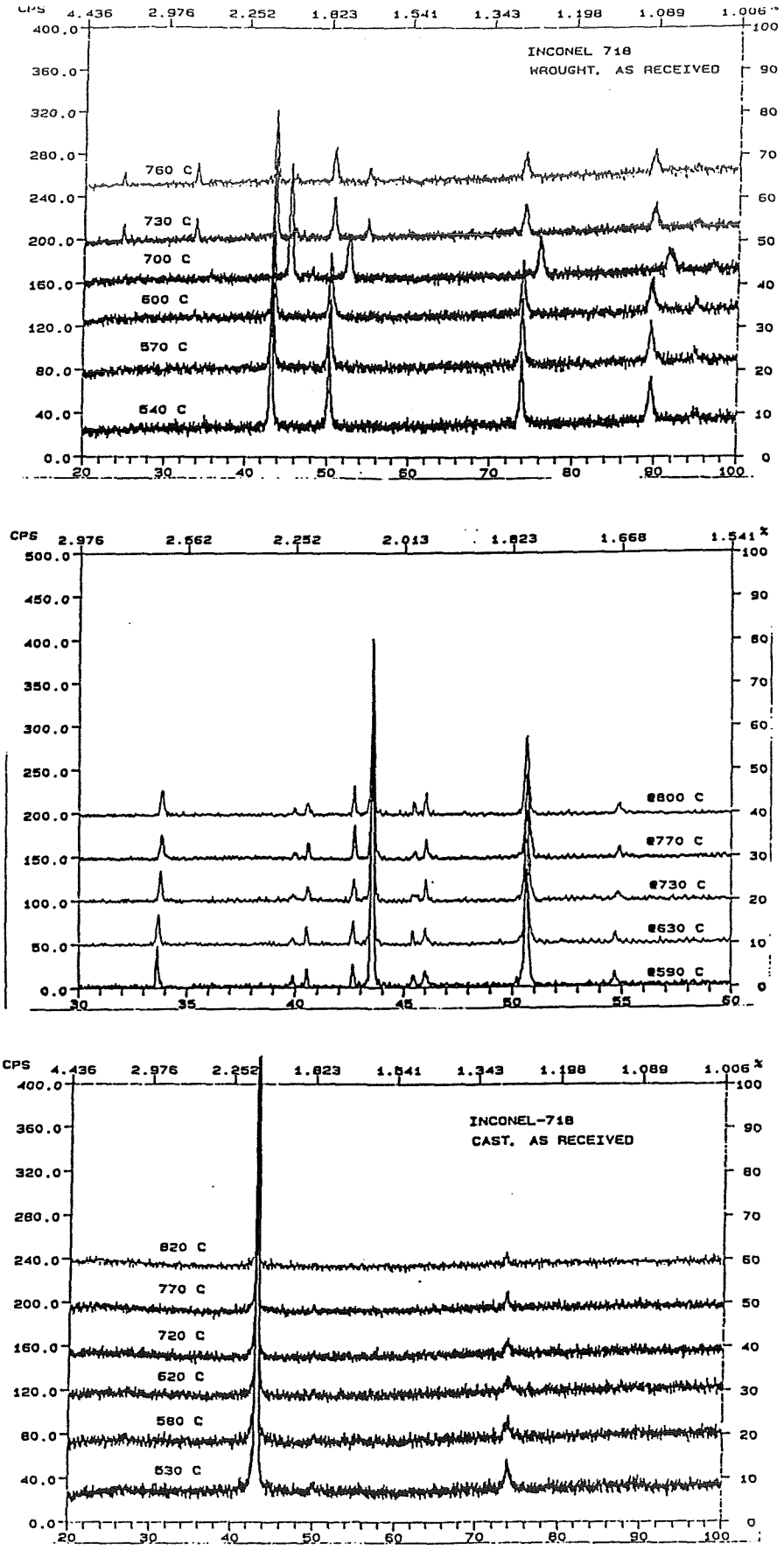

Figure 7. High temperature x-ray diffraction of scans of wrought Inconel 718.

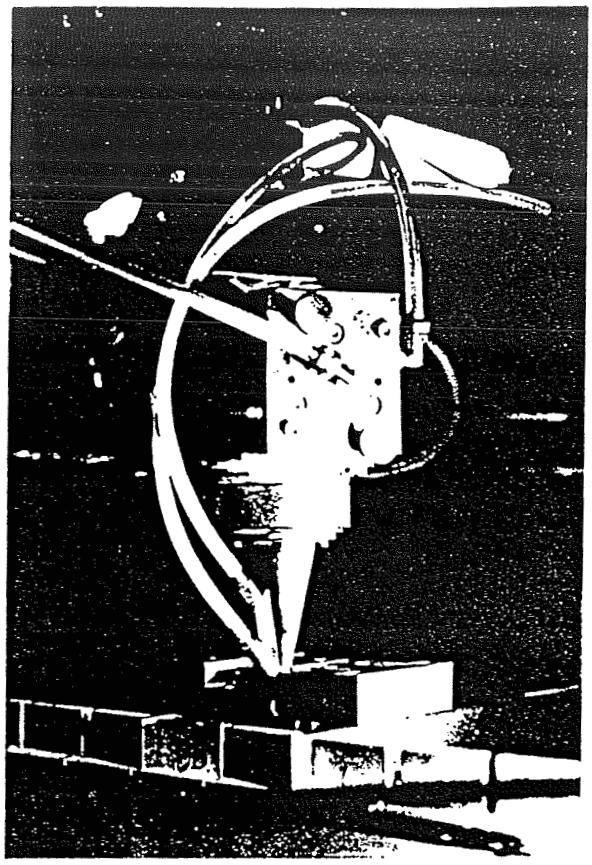

Figure 8. Welding fixture at nozzle.

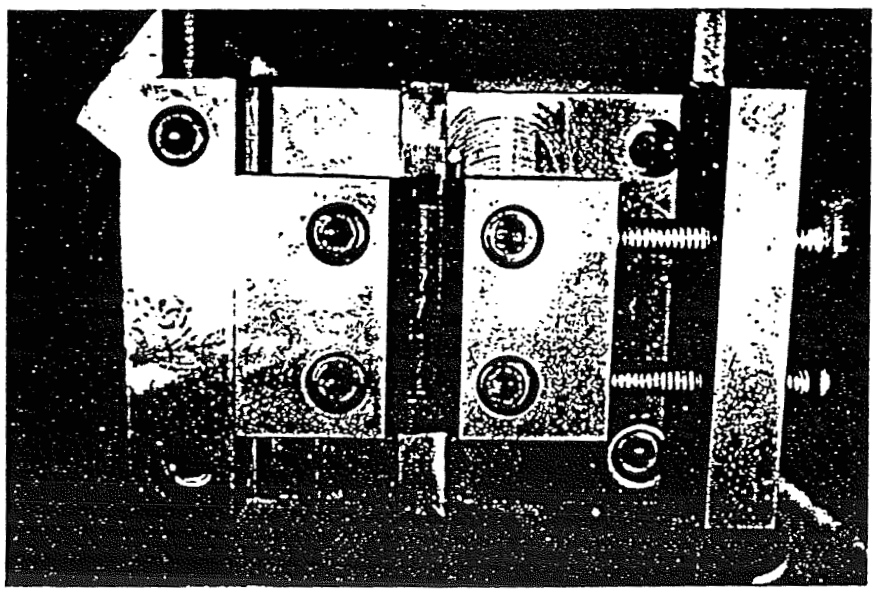

Figure 9. Welding fixture.

Mixed Frequency Pulsing (5kHz pulse width modulation on/Gated pulse on)

Pulse On Time = 35 ms
Pulse Off Time = 60 ms
Gate Duty Cycle = 37%
5kHz PWM Duty Cycle 50%

Peak Power 370 W
Pulse Average Power = 1850 W
Mixed Frequency Average Power 685 W

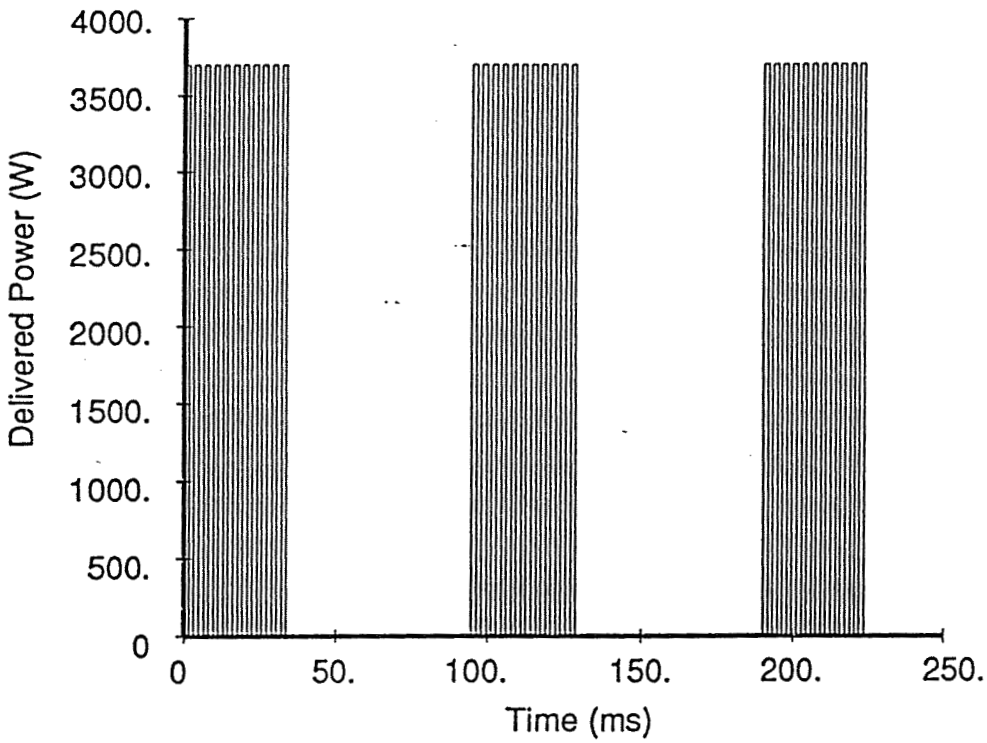

Figure 10. Mixed frequency pulsing format.

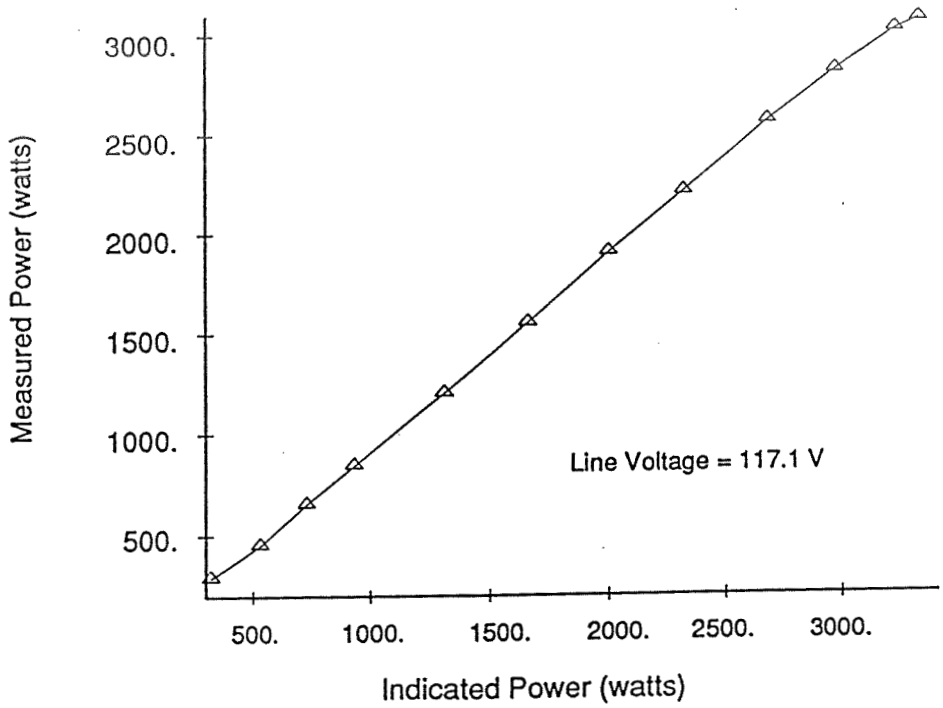

Figure 11. Results of laser power calibration.

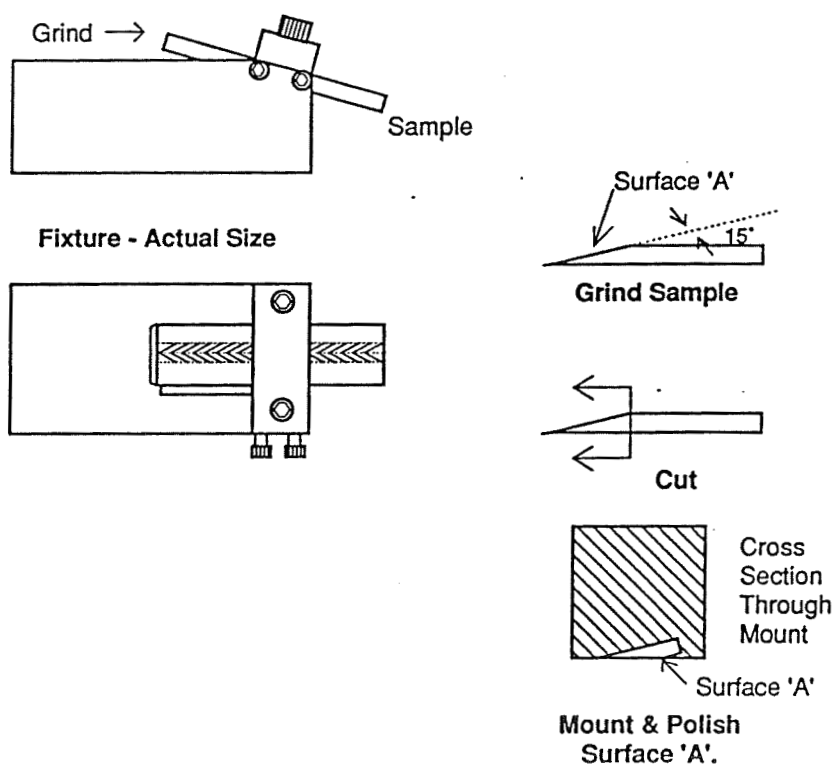

Figure 12. Preparation of slant-grind specimens.

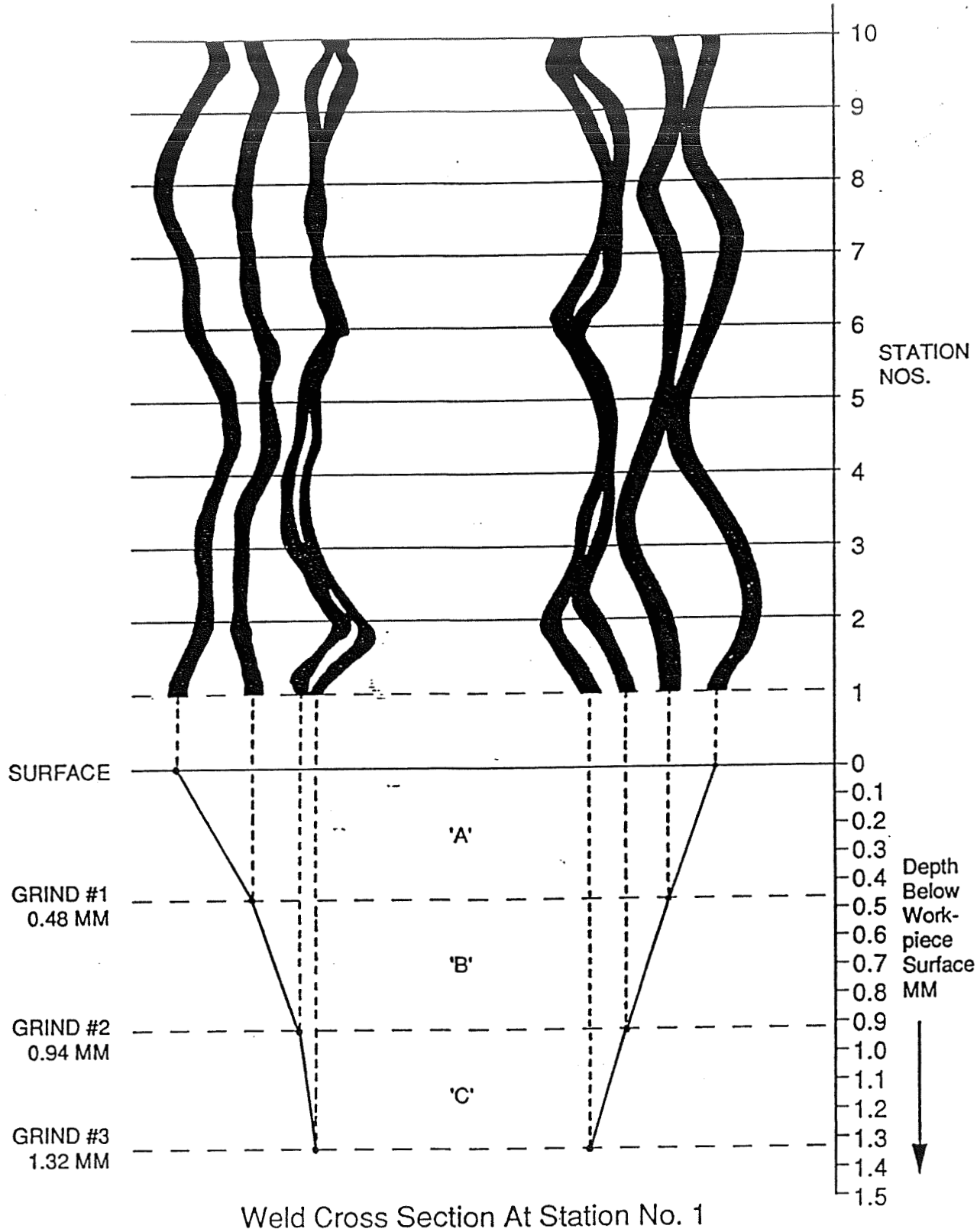

Figure 13. Transverse curvature measurement.

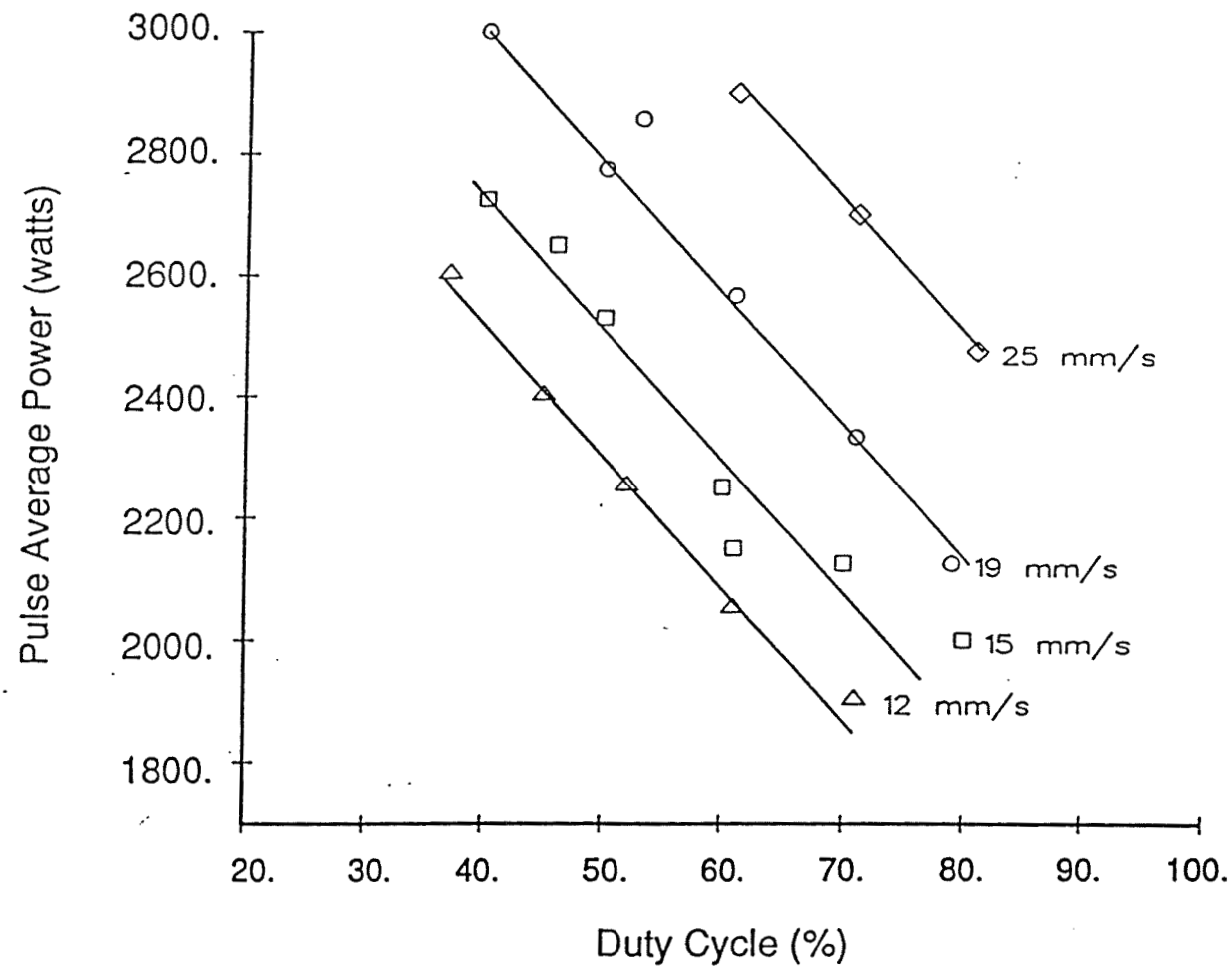

Figure 14. Unrestrained welds having full penetration - welded at four speeds.

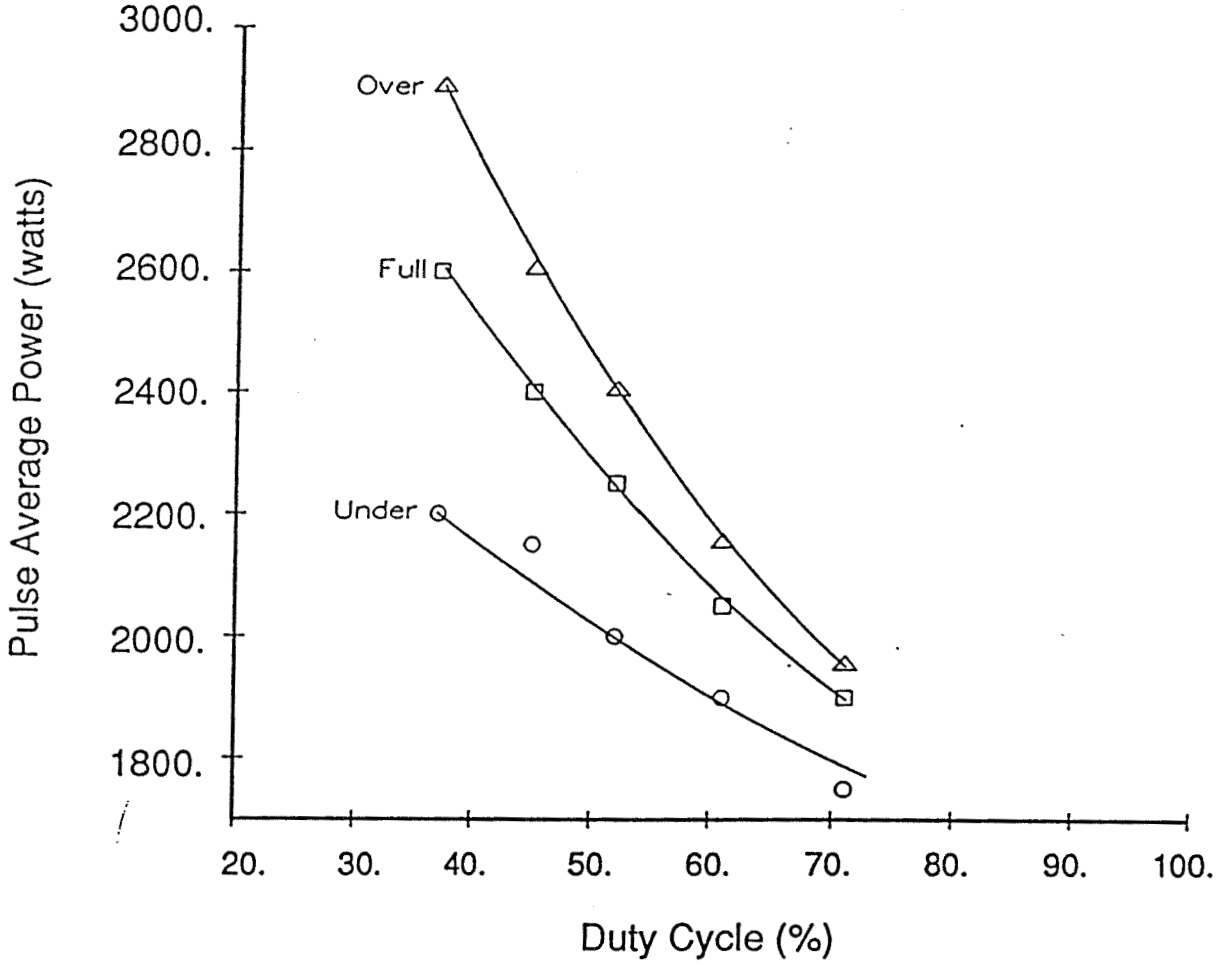

Figure 15. Penetration as it relates to pulse average power and duty cycle.

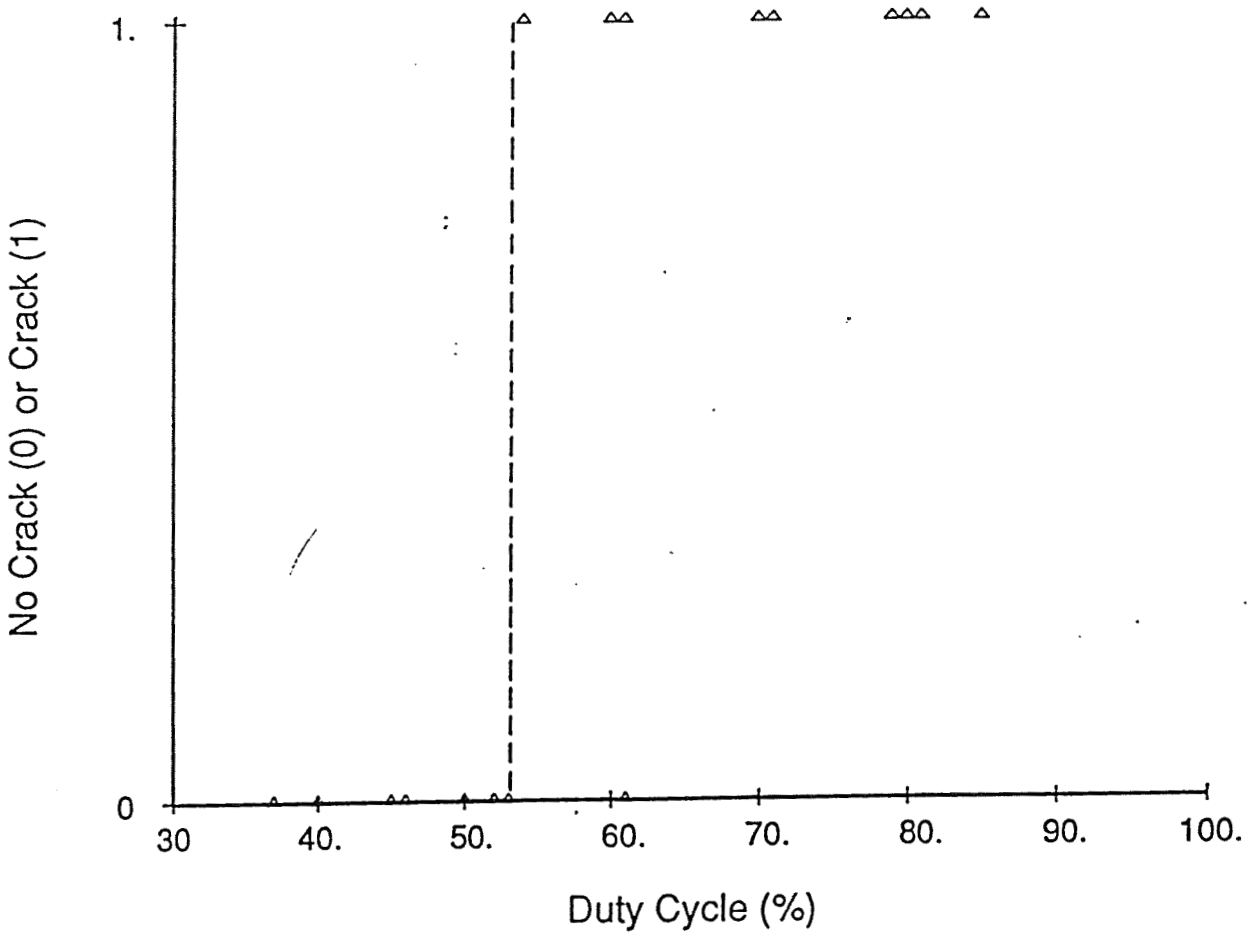

Figure 16. Centerline cracking as it relates to duty cycle in unrestrained welds.

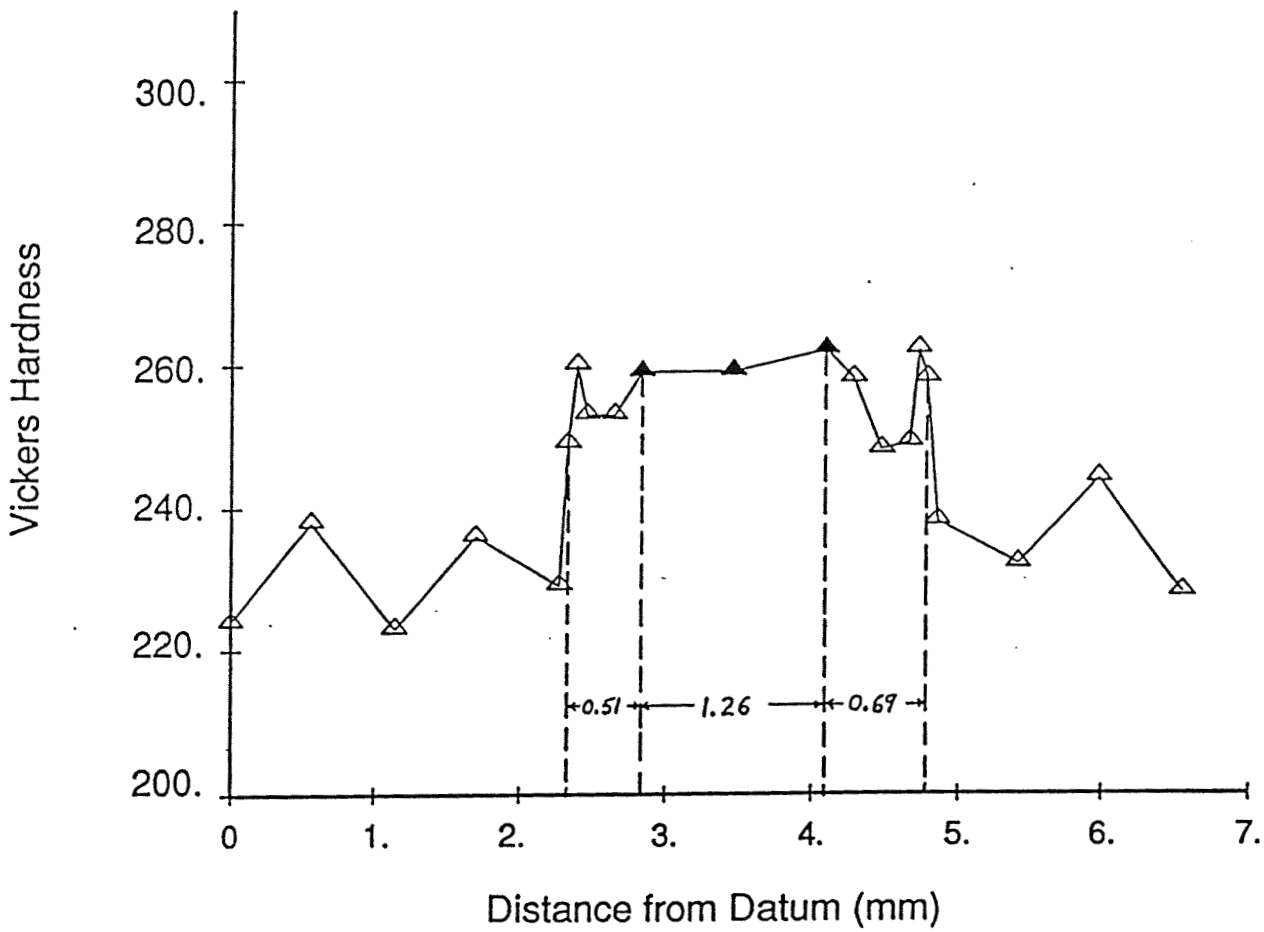

Figure 17. HAZ measurement for sample U9, 61% duty cycle, 2567 watts, speed 18 mm/s (Darkened points visually determined to be in fusion zone).

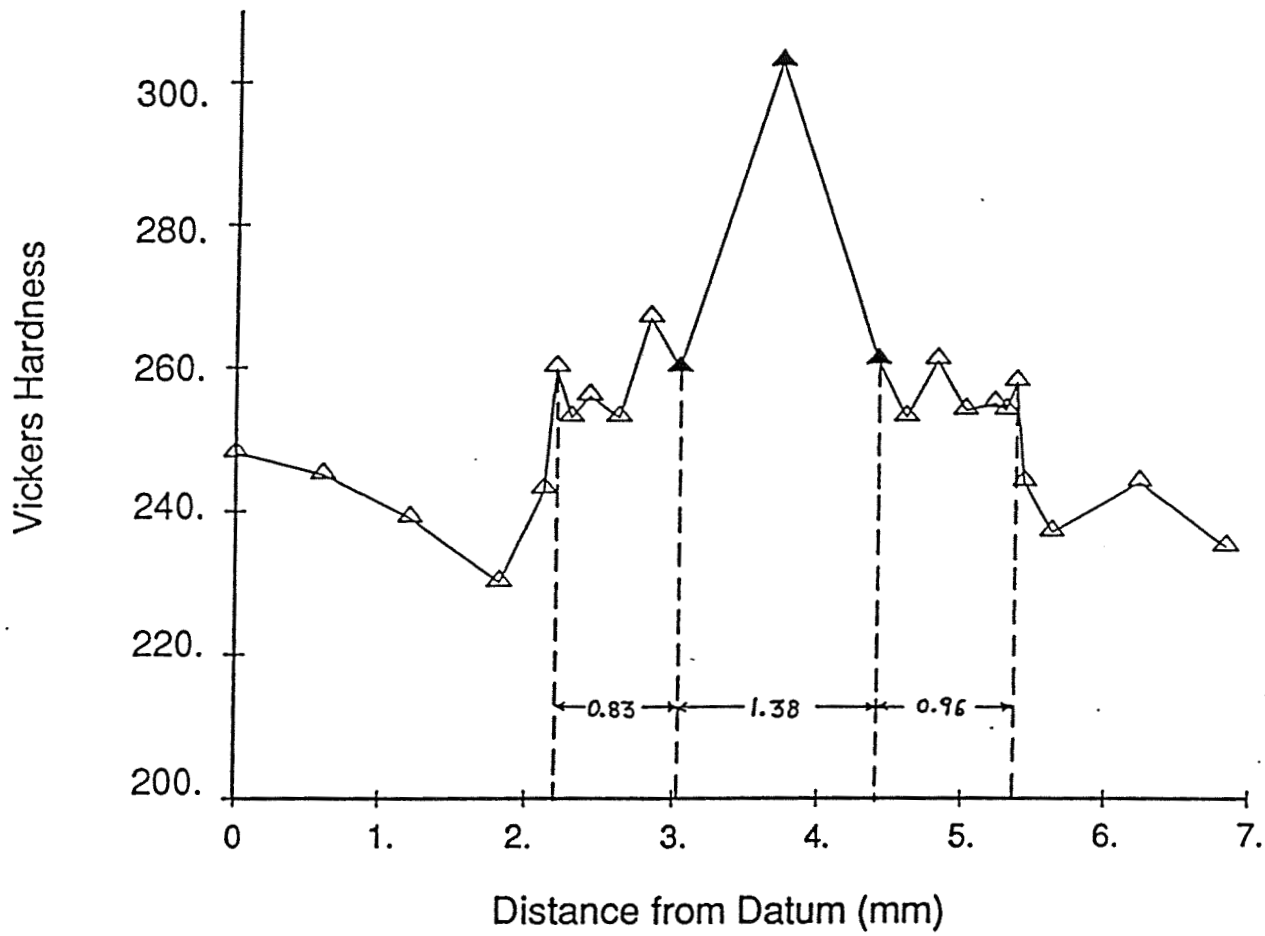

Figure 18. HAZ measurement for sample U28, 71% duty cycle, 1900 watts, speed 12 mm/s (Darkened points visually determined to be in fusion zone).

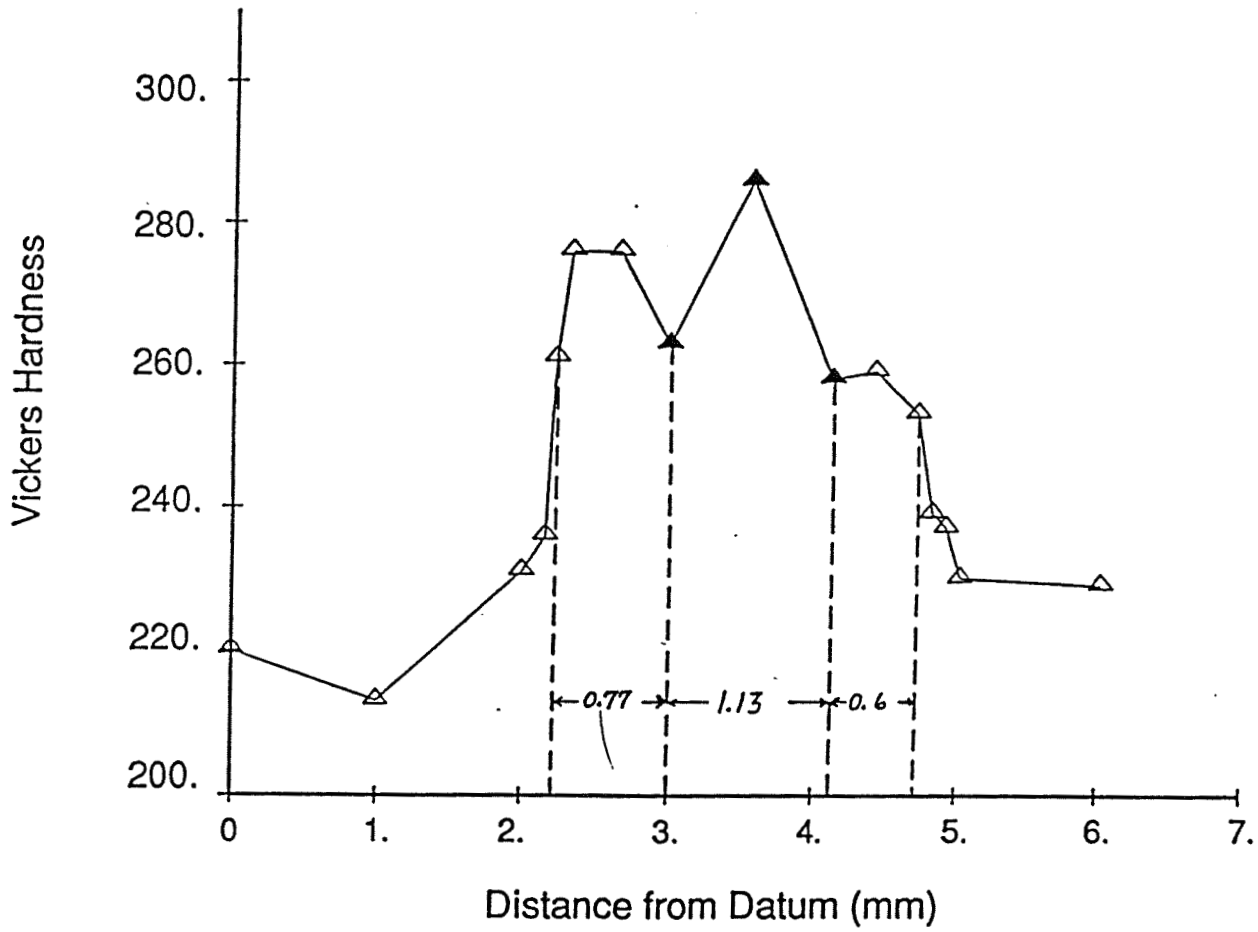

Figure 19. HAZ measurement for a CW weld, 2500 watts, speed 25 mm/s (Darkened points visually determined to be in fusion zone).

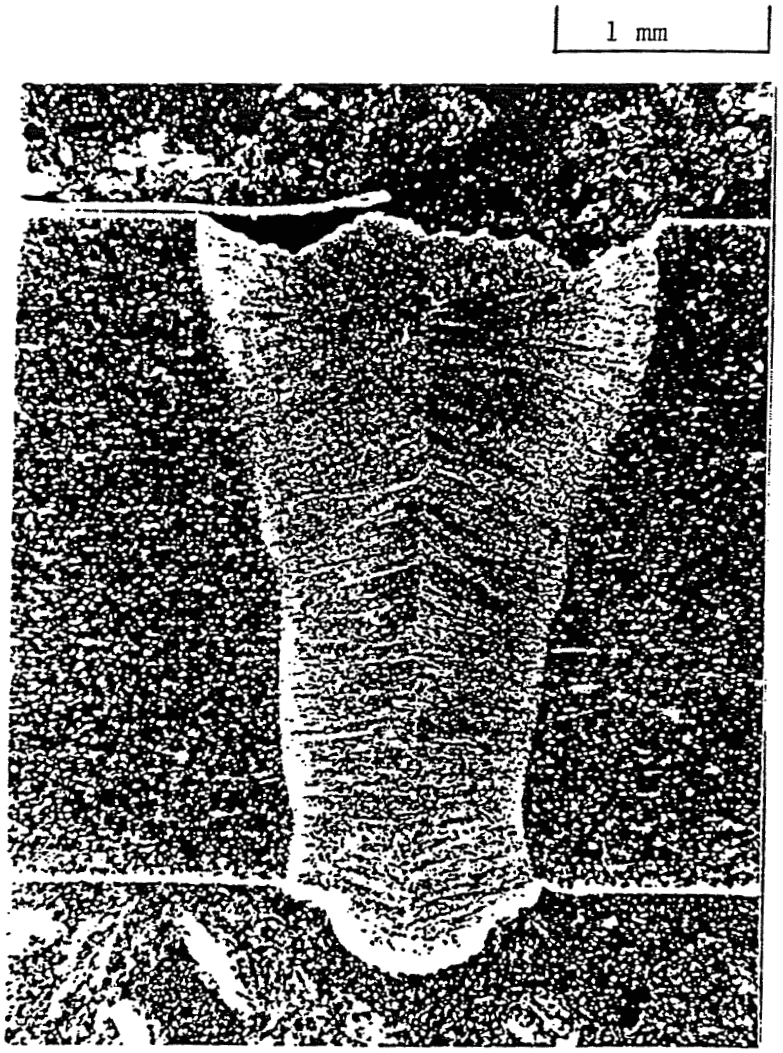

Figure 20. Fully penetrated restrained weld, 2250 watts, 61 percent duty cycle (Condition R13).

ORIGINAL PAGE IS
OF POOR QUALITY

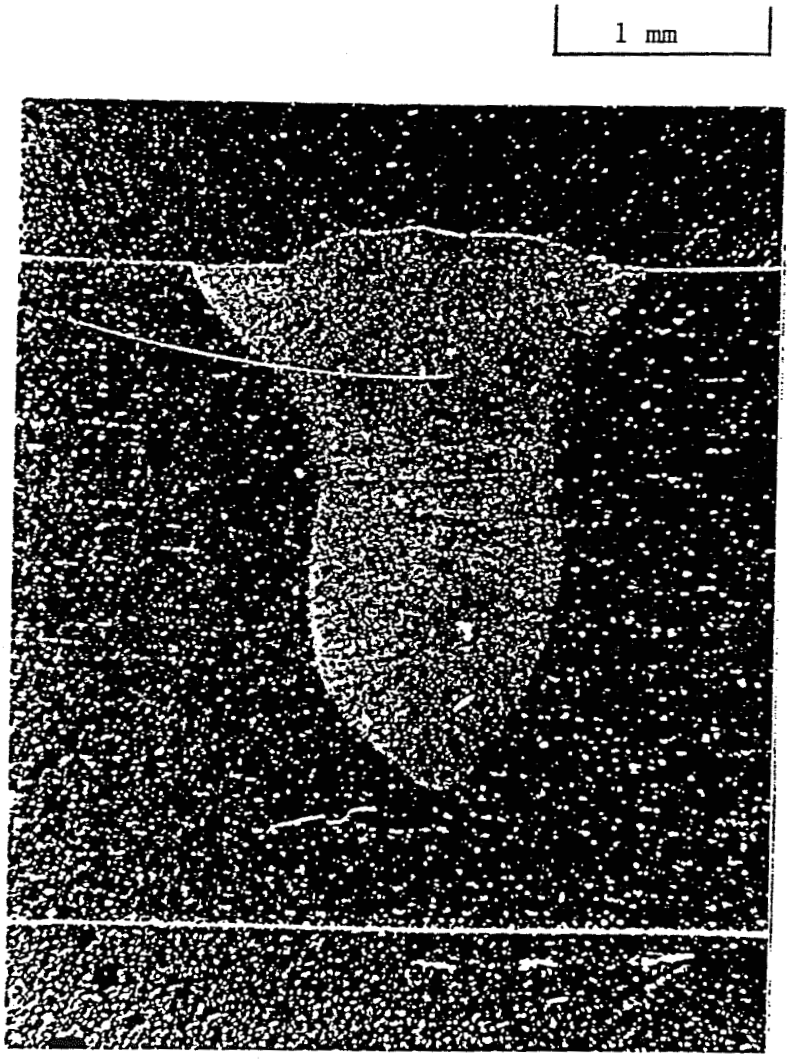

Figure 21. Underpenetrated restrained weld, 2050 watts, 37 percent duty cycle (Condition R10).

ORIGINAL PAGE IS
OF POOR QUALITY

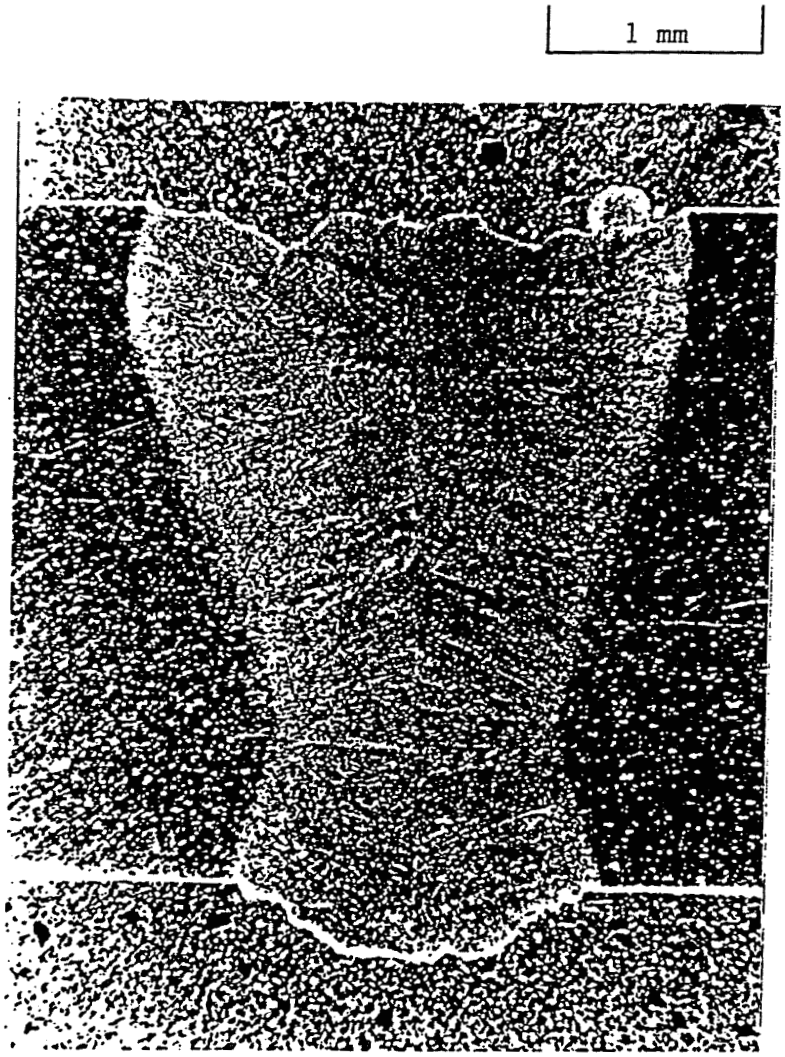

Figure 22. Overpenetrated restrained weld, 2600 watts, 71 percent duty cycle (Condition R17).

ORIGINAL PAGE IS
OF POOR QUALITY

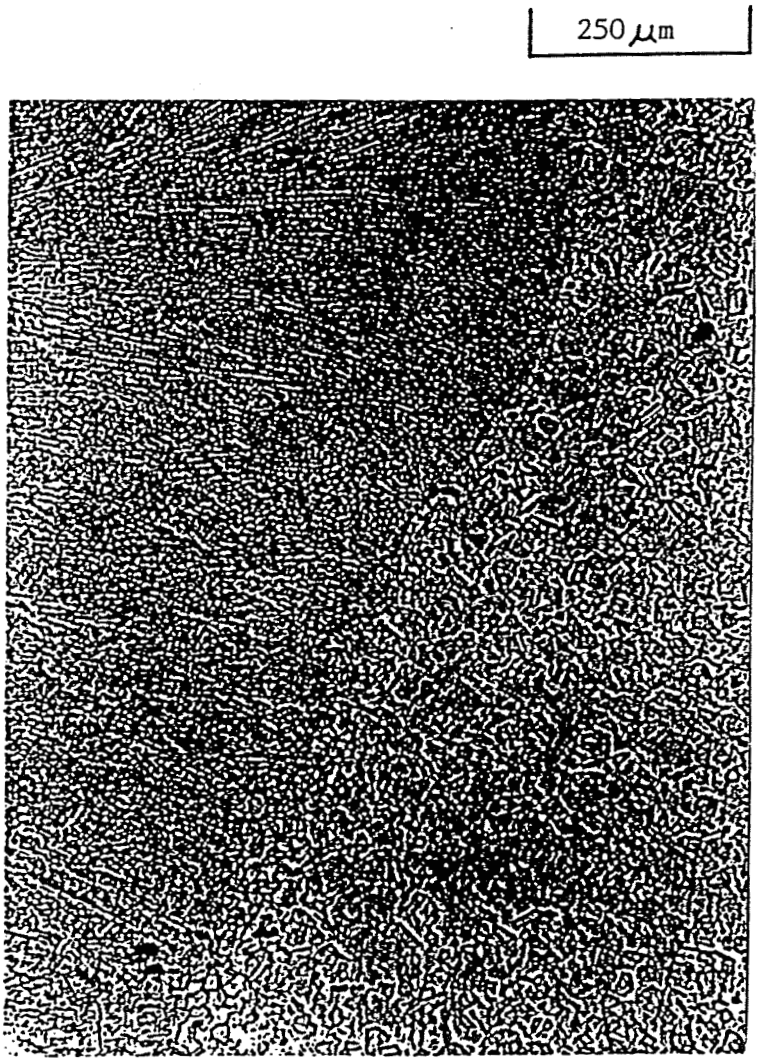

Figure 23. Typical view of weld nailhead/HAZ interface for Condition R6 (2050 watts, 80 percent duty cycle).

ORIGINAL PAGE IS
OF POOR QUALITY

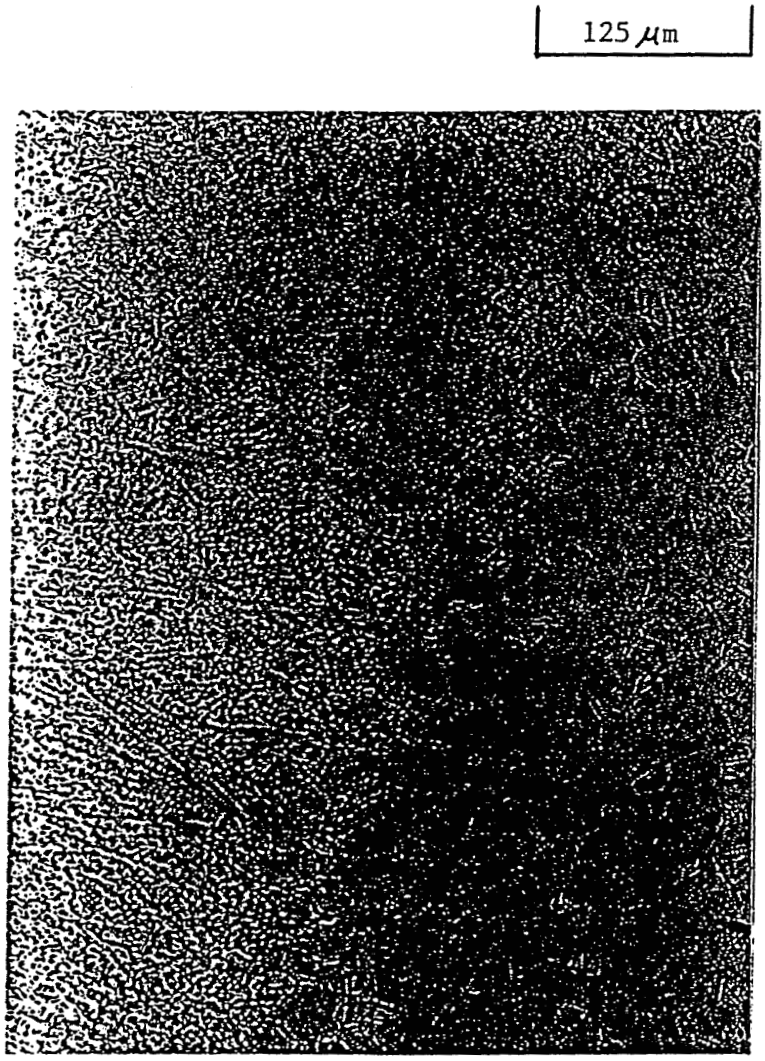

Figure 24. Weld nailhead showing weld structure and grain boundaries for Condition R6 (2050 watts, 80 percent duty cycle).

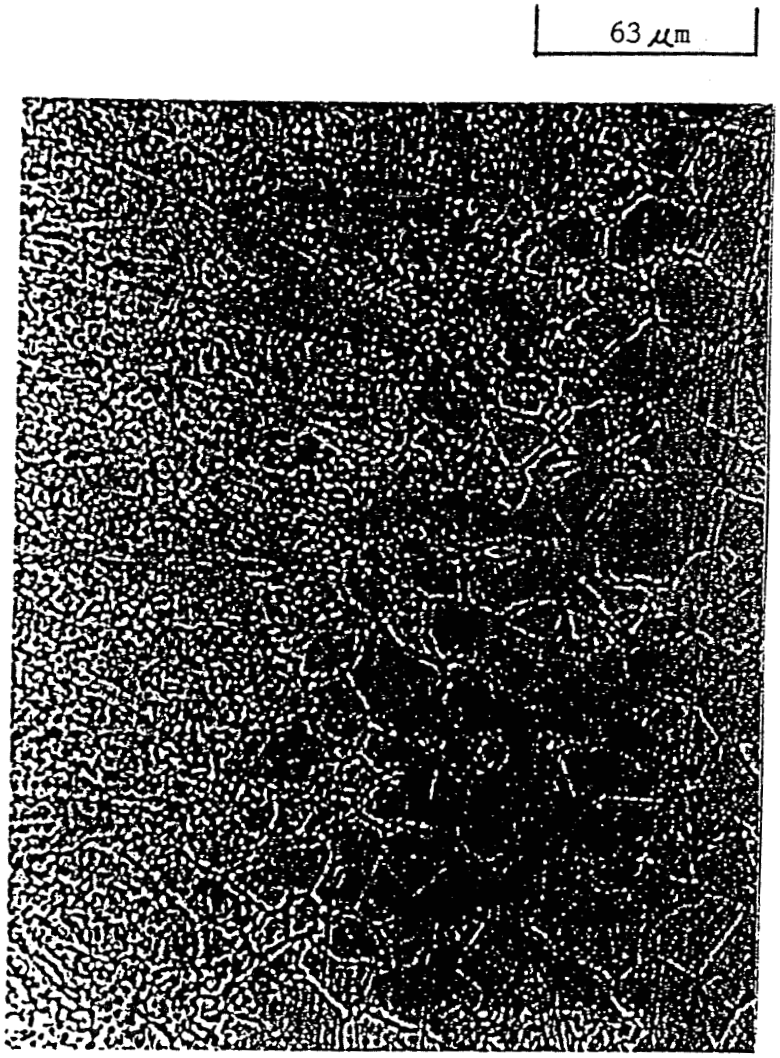

Figure 25. Typical weld HAZ - note the dark grain boundary precipitates. Condition R6 (2020 watts, 80 percent duty cycle).

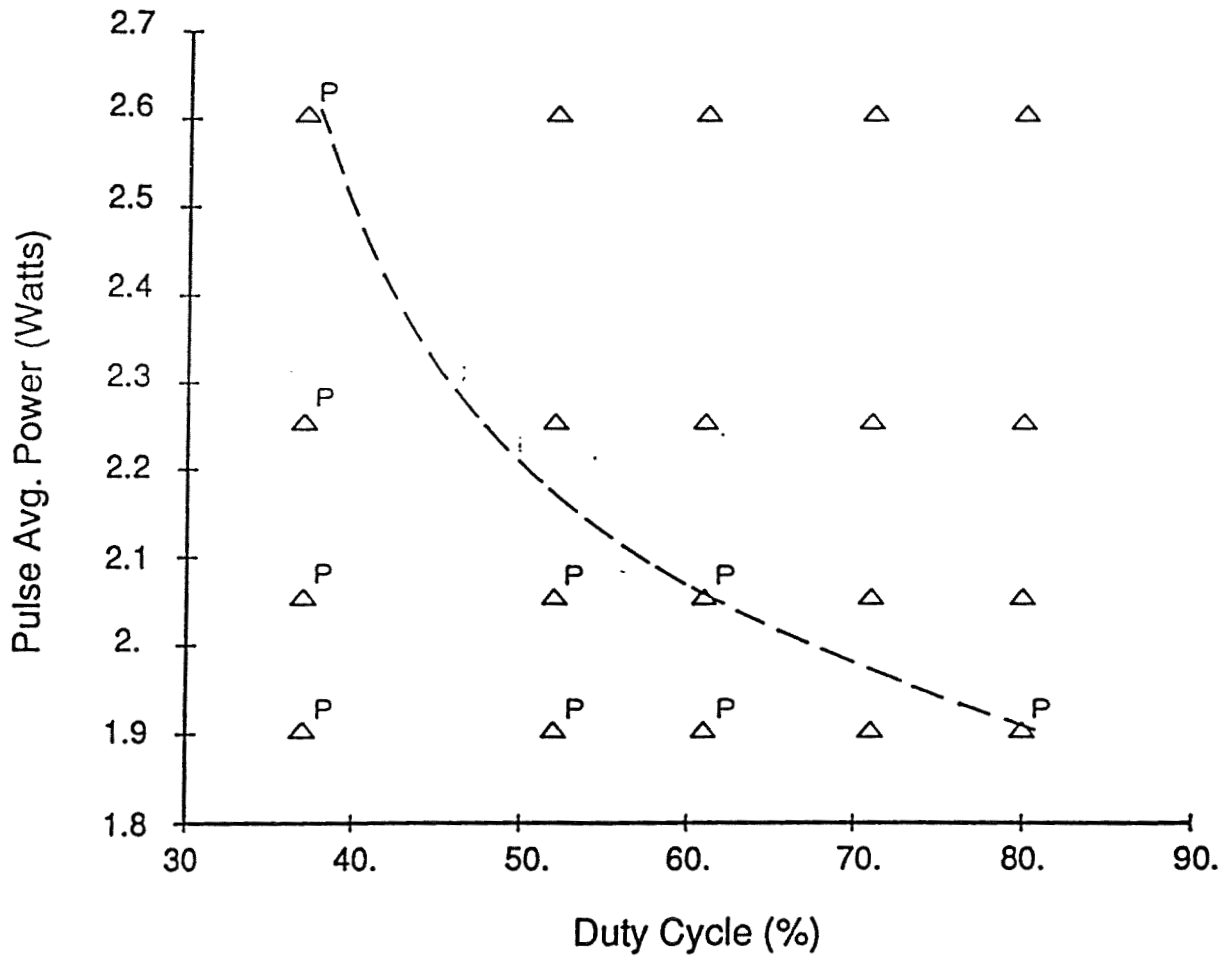

Figure 26. Restrained weld matrix (P indicates samples containing pores).

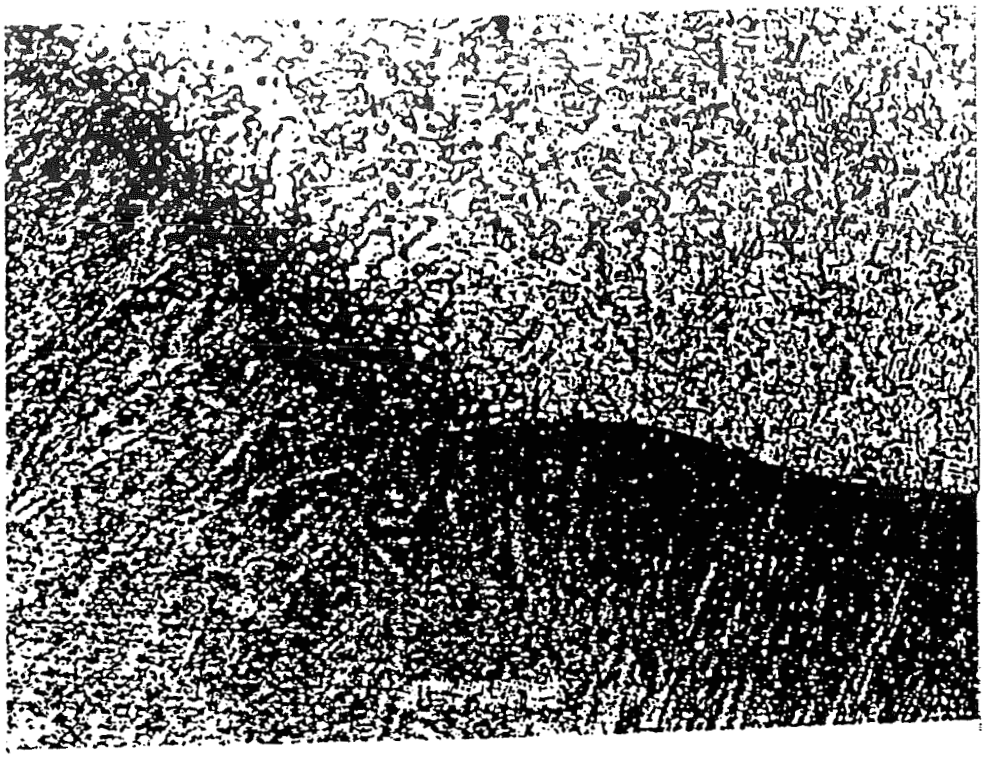

(a)

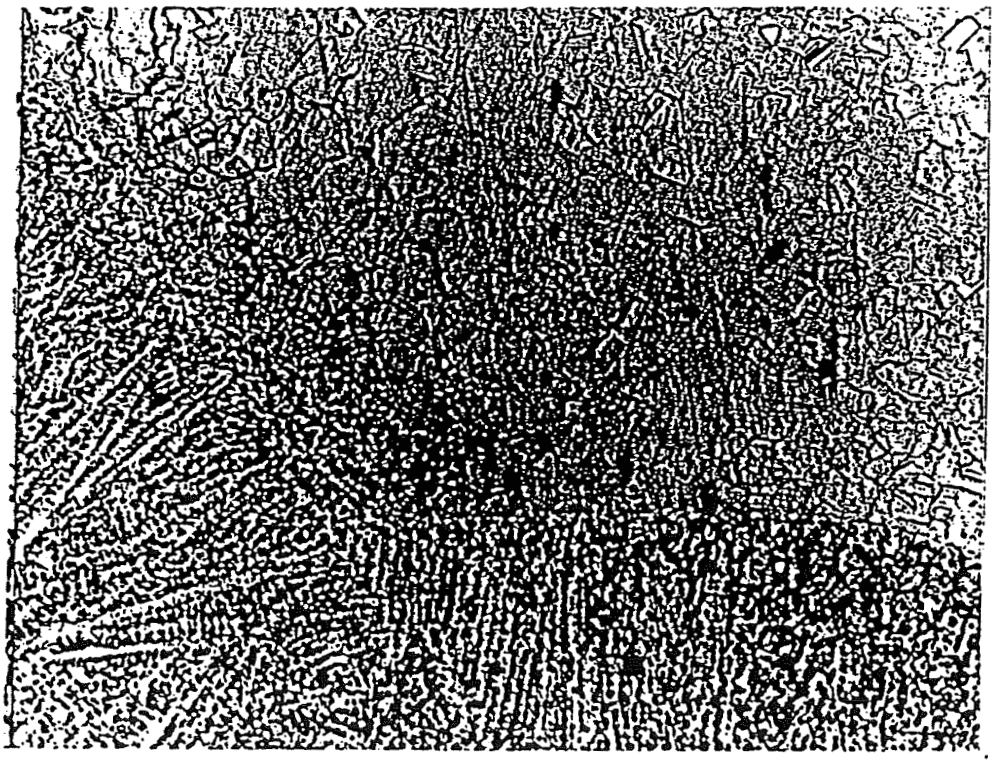

(b)

Figure 27. Microstructure of wrought IN 718 in the region of the nailhead (a) 100X and (b) 200X.

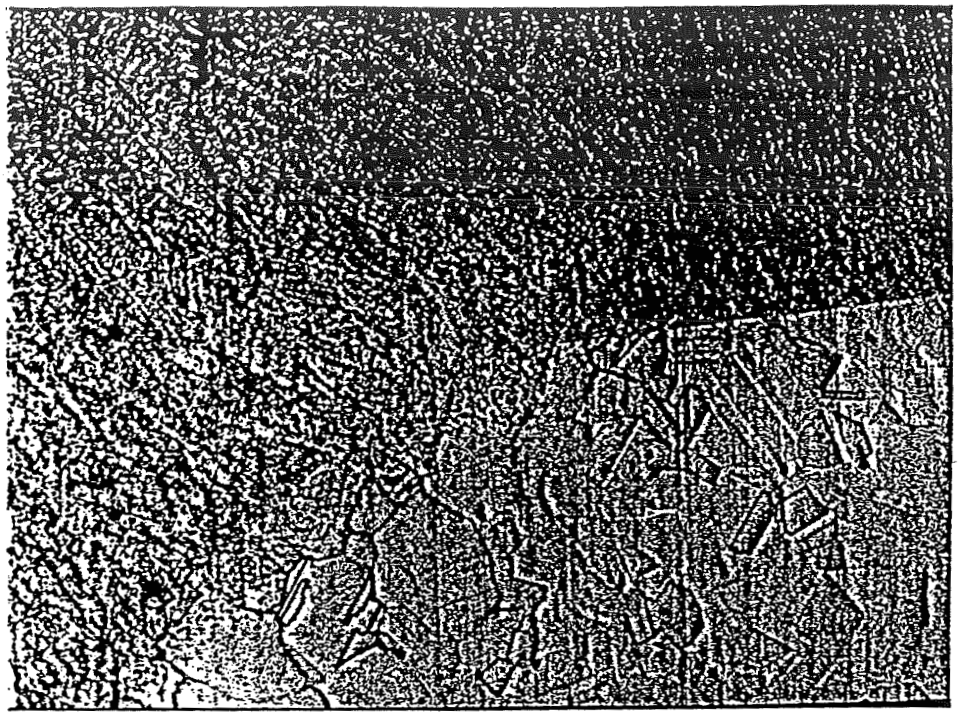

(a)

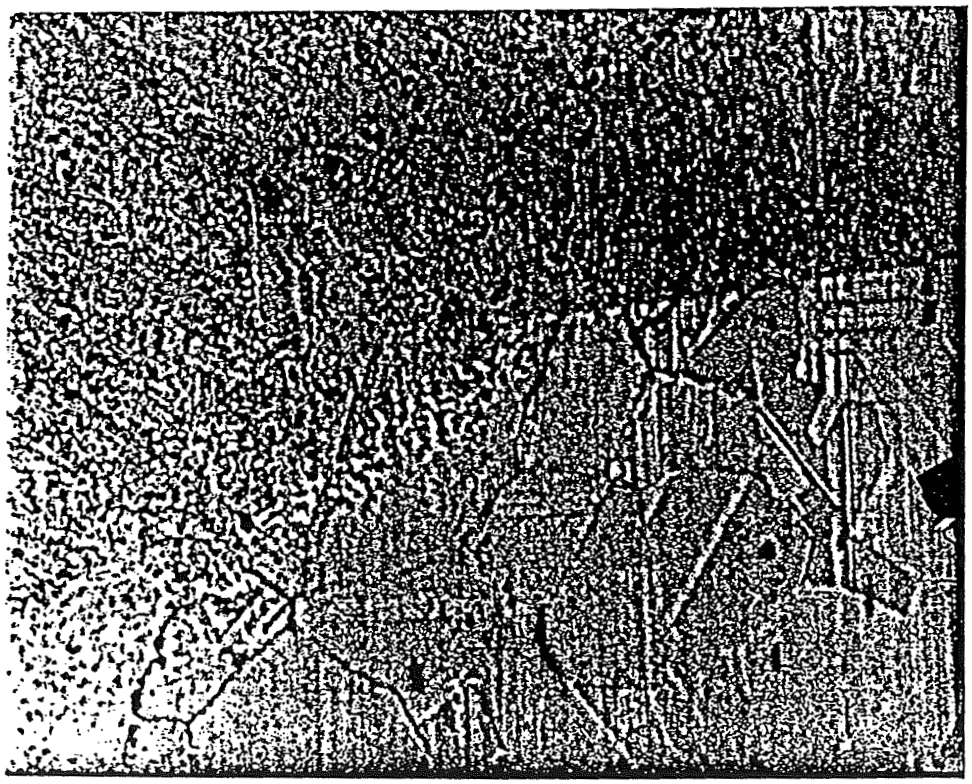

(b)

Figure 28. Microstructure of wrought grain grown IN 718 in the region of the nailhead (a) 100X and (b) 200X.

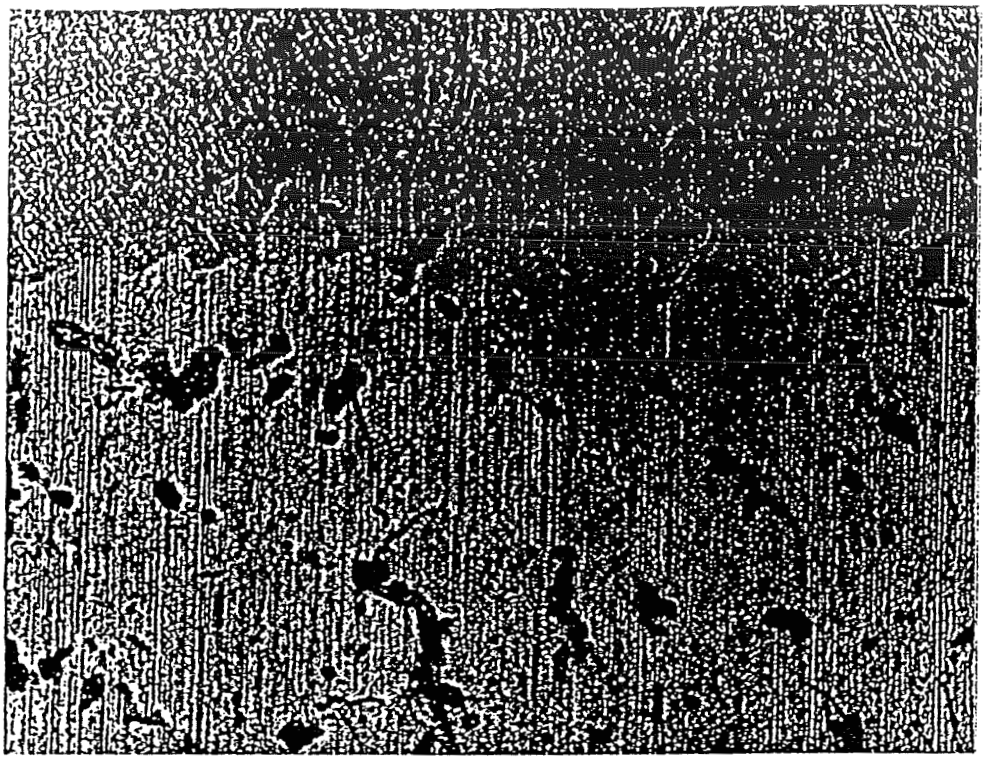

(a)

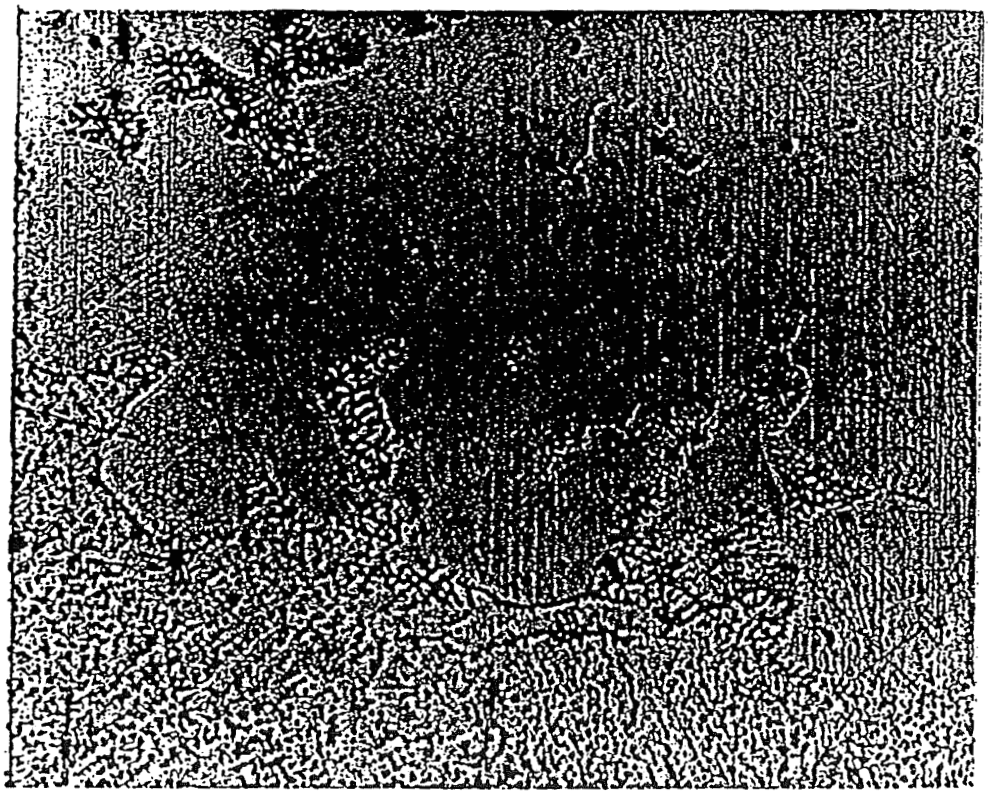

(b)

Figure 29. Microstructure of cast IN 718 in the region of the nailhead (a) 100X and (b) 200X.